

2. EXPLANATORY NOTES¹

Shipboard Scientific Party²

INTRODUCTION

In this chapter, we have assembled information that will help the reader understand the basis for our preliminary conclusions and also help the interested investigator select samples for further analysis. This information concerns only shipboard operations and analyses described in the site reports in the *Initial Reports* volume of the Leg 138 *Proceedings of the Ocean Drilling Program*. Methods used by various investigators for shore-based analyses of Leg 138 data will be detailed in the individual scientific contributions published in the *Scientific Results* volume.

Authorship of Site Chapters

The separate sections of the site chapters were written by the following shipboard scientists (authors are listed in alphabetical order, no seniority is implied):

Site Summary: Mayer, Pisias
Background and Scientific Objectives: Mayer, Pisias
Operations: Grout, Janecek
Lithostratigraphy: Hagelberg, Hovan, Kemp, Leinen, Levitan, Mix, Ravelo
Biostratigraphy: Baldauf, Flores, Iwai, Moore, Raffi, Shackleton, Vincent
Paleomagnetism: Levi, Schneider, Valet
Sediment Accumulation Rates: Hagelberg, Shackleton
Inorganic Geochemistry: Farrell, Klinkhammer
Organic Geochemistry: Emeis, Galimov
Physical Properties: Holler, Kim, McKillop, Meynardier
Downhole Measurements: Dadey, Lyle
Summary and Conclusions: Mayer, Pisias
Appendix: Shipboard Scientific Party

Following the text of the site chapter are summary core descriptions ("barrel sheets") and photographs of each core.

Use of "Ma" vs. "m.y."

1. *Ma* is equivalent to and replaces m.y.B.P. (million years Before Present), for example, 35–40 Ma.
2. *m.y.* is used in sentences such as ". . . for 5 m.y. in the early Miocene."

Drilling Characteristics

Information concerning sedimentary stratification in uncored or unrecovered intervals may be inferred from seismic data, wireline-logging results, and from an examination of the behavior of the drill string, as observed and recorded on the drilling platform. Typically, the harder a layer, the slower and more difficult it is to penetrate. A number of other factors may determine the rate of penetration, so it

is not always possible to relate the drilling time directly to the hardness of the layers. Bit weight and revolutions per minute, recorded on the drilling recorder, also influence the penetration rate.

Drilling Deformation

When cores are split, many show signs of significant sediment disturbance, including the concave-downward appearance of originally horizontal bands, haphazard mixing of lumps of different lithologies (mainly at the tops of cores), and the near-fluid state of some sediments recovered from tens to hundreds of meters below the seafloor. Core deformation probably occurs during cutting, retrieval (with accompanying changes in pressure and temperature), and core handling on deck.

Shipboard Scientific Procedures

Numbering of Sites, Holes, Cores, and Samples

ODP drill sites are numbered consecutively and refer to one or more holes drilled while the ship was positioned over one acoustic beacon. Multiple holes may be drilled at a single site by pulling the drill pipe above the seafloor (out of the hole), moving the ship some distance from the previous hole, and then drilling another hole.

For all ODP drill sites, a letter suffix distinguishes each hole drilled at the same site. For example, the first hole drilled is assigned the site number modified by the suffix "A," the second hole takes the site number and suffix "B," and so forth. Note that this procedure differs slightly from that used by DSDP (Sites 1 through 624), but prevents ambiguity between site- and hole-number designations. It is important to distinguish among holes drilled at a site, because recovered sediments or rocks from different holes usually do not come from equivalent positions in the stratigraphic column.

The cored interval is measured in meters below seafloor (mbsf). The depth interval assigned to an individual core begins with the depth below the seafloor that the coring operation began, and extends to the depth that the coring operation ended (see Fig. 1). For example, each coring interval is generally up to 9.5 m long, which is the length of a core barrel. Coring intervals may be shorter and may not necessarily be adjacent if separated by drilled intervals. In soft sediments, the drill string can be "washed ahead" with the core barrel in place, without recovering sediments. This is achieved by pumping water down the pipe at high pressure to wash the sediment out of the way of the bit and up the space between the drill pipe and the wall of the hole. If thin, hard, rock layers are present, then it is possible to get "spotty" sampling of these resistant layers within the washed interval and thus to have a cored interval greater than 9.5 m. When drilling hard rock, a center bit may replace the core barrel if it is necessary to drill without core recovery.

Cores taken from a hole are numbered serially from the top of the hole downward. Core numbers and their associated cored intervals in meters below seafloor usually are unique in a given hole; however, this may not be true if an interval is cored twice, if the borehole wall caves in, or other hole problems occur. Maximum full recovery for a single core is 9.5 m of rock or sediment contained in a plastic liner (6.6 cm internal diameter) plus about 0.2 m (without a plastic liner) in the core catcher (Fig. 2). The core catcher is a device at the bottom of the core barrel that prevents the core from sliding out when the

¹ Mayer, L., Pisias, N., Janecek, T., et al., 1992. *Proc. ODP, Init. Repts.*, 138: College Station, TX (Ocean Drilling Program).

² Shipboard Scientific Party is as given in list of participants preceding the contents.

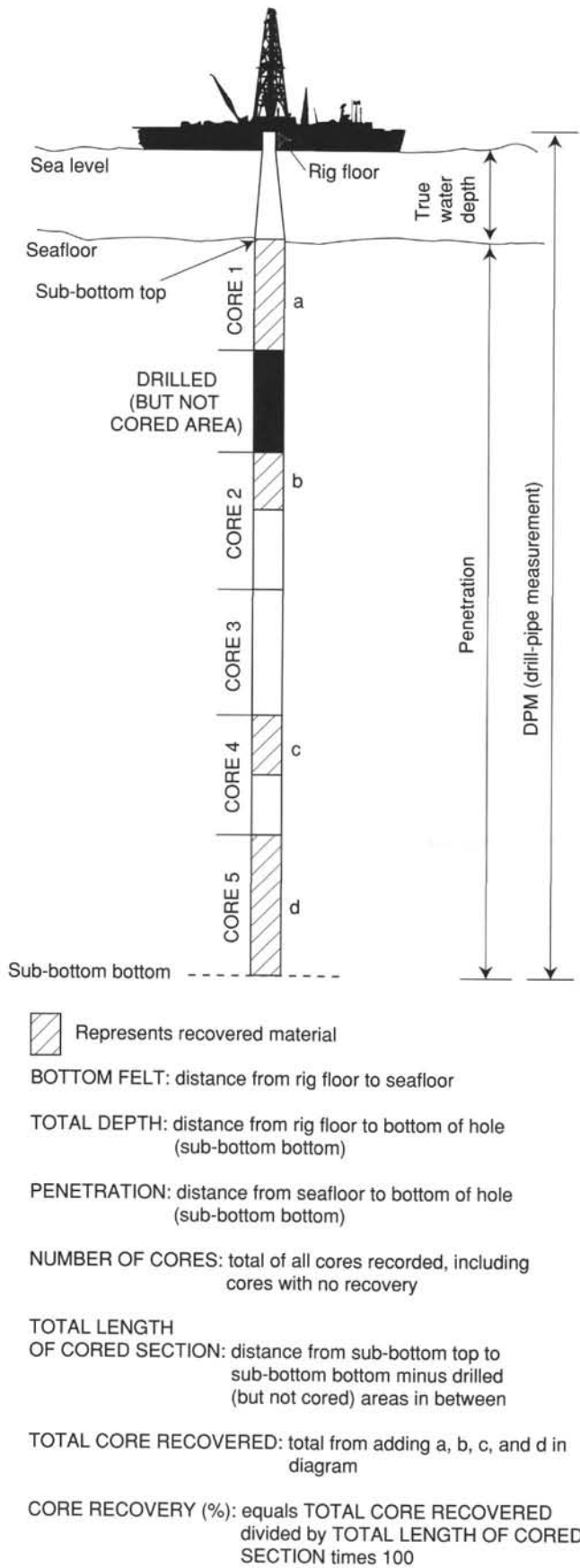


Figure 1. Coring and depth intervals.

barrel is being retrieved from the hole. In many APC/XCB cores, recovery exceeds the 9.5-m maximum by as much as 0.60 m. The cause of this expansion is not fully understood (see Hagelberg et al., this volume).

A recovered core is divided into 1.5-m sections that are numbered serially from the top (Fig. 2). When full recovery is obtained, the sections are numbered from 1 through 7, with the last section possibly being shorter than 1.5 m (rarely, an unusually long core may require more than seven sections). When less than full recovery is obtained, as many sections as are needed to accommodate the length of the core will be recovered; for example, 4 m of core would be divided into two 1.5-m sections and a 1-m section. If cores are fragmented (recovery less than 100%), sections are numbered serially and intervening sections are noted as void, whether shipboard scientists believe that the fragments were contiguous *in-situ* or not. In rare cases, a section less than 1.5 m may be cut to preserve features of interest (e.g., lithological contacts).

By convention, material recovered from the core catcher is placed below the last section when the core is described and is labeled core catcher (CC); in sedimentary cores, it is treated as a separate section. The core catcher is placed at the top of the cored interval in cases where material is only recovered in the core catcher. However, information supplied by the drillers or by other sources may allow for more precise interpretation as to the correct position of core-catcher material within an incompletely recovered cored interval.

When the recovered core is shorter than the cored interval, the top of the core is equated with the top of the cored interval by convention, to achieve consistency when handling analytical data derived from the cores (see Hagelberg et al., this volume, for more information about depth assignment to individual cores during Leg 138). Samples removed from the cores are designated by distance, measured in centimeters from the top of the section to the top and bottom of each sample removed from that section.

A complete identification number for a sample consists of the following information: leg, site, hole, core number, core type, section

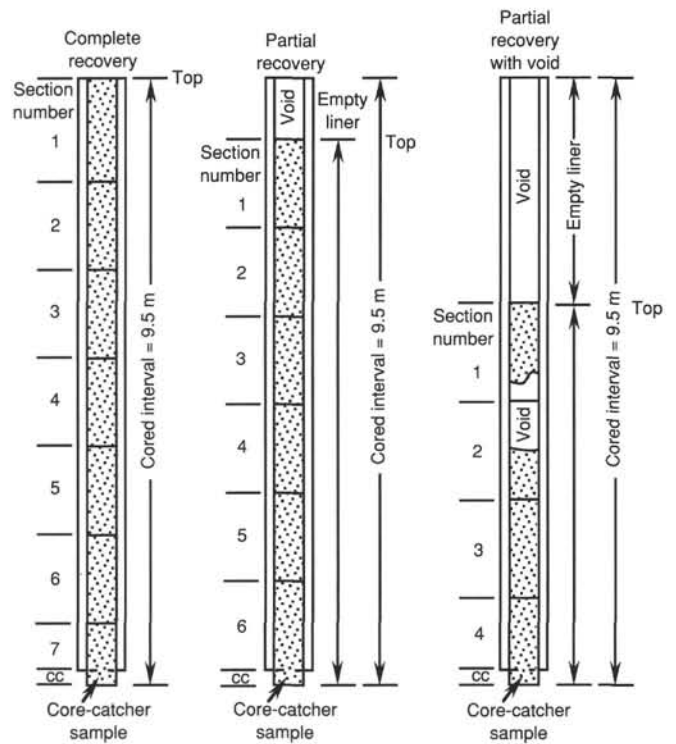


Figure 2. Examples of numbered core sections.

number, piece number (for hard rock), and interval in centimeters, measured from the top of section. For example, a sample identification of "138-844A-15H-1, 10–12 cm" would be interpreted as representing a sample removed from the interval between 10 and 12 cm below the top of Section 1, Core 15 (H designates that this core was taken by the advanced piston corer) of Hole 844A during Leg 138.

All ODP core and sample identifiers indicate core type. The following abbreviations are used: R = rotary core barrel (RCB); H = hydraulic piston core (HPC; also referred to as APC, or advanced hydraulic piston core); P = pressure core barrel; X = extended core barrel (XCB); B = drill-bit recovery; C = center-bit recovery; I = *in situ* water sample; S = sidewall sample; W = wash-core recovery; and M = miscellaneous material. Only APC, XCB, and W cores were cut during Leg 138.

Core Handling

As soon as a core was retrieved on deck, a sample taken from the core catcher was given to the paleontological laboratory for an initial age assessment. Special care was taken in transferring the core from the drill floor to a long horizontal rack on a catwalk near the core laboratory so that the core did not bend or twist excessively. The core was capped immediately, and gas samples were taken by piercing the core liner and withdrawing gas into a vacuum tube. Voids within the core were sought as sites for gas sampling. Some of the gas samples were taken from the end of cut sections on the catwalk and sealed in glass vials for light hydrocarbon analysis. Afterward, each section was sealed at the top and bottom by gluing on color-coded plastic caps: blue to identify the top of a section and clear for its bottom. A yellow cap was placed on the section ends from which a whole-round sample was removed. The caps were usually attached to the liner by coating the end liner and the inside rim of the cap with acetone and then attaching the caps to the liners.

The cores were then carried into the laboratory, where the sections were labeled with an engraver to mark the complete designation of the section permanently. The length of the core in each section and the core-catcher sample were measured to the nearest centimeter. This information was logged into the shipboard CORELOG data-base program.

Whole-round sections from APC and XCB cores normally were run through the multisensor track (MST). The MST includes the gamma-ray attenuation porosity evaluator (GRAPE), the *P*-wave logger, and a volume magnetic susceptibility meter. Prior to MST analysis, the temperature of each core was measured. After the core had equilibrated to room temperature (approximately 3 hr), soft sediments were measured for thermal conductivity prior to being split. Cores were split lengthwise into working and archive halves. Softer cores were split with a wire. Harder cores were split using a diamond saw. The wire-cut cores were split from the top to bottom so that sediment below the voids or soupy intervals that were sometimes present at the top of Section 1 would not be drawn into the voids.

After splitting, working and archive halves of each section were designated. The archive halves of cores were first scraped gently across to expose a smooth, fresh surface for description and color analysis. Scrapings were saved for XRF and other analyses. Archive halves then were described visually. Smear slides were made from samples taken from the archive half. Archive halves were then analyzed using an automated color analysis system that measured and recorded the percentage of light reflected from the core in 1-nm-wavelength

bands from 450 to 950 nm. These color measurements were conducted at intervals ranging from 1 to 8 cm (see Mix et al., this volume). This analysis was followed by our running the archive half of the core through the cryogenic magnetometer. Finally, the cores were photographed with both black-and-white and color film, a whole core at a time. Close-up photographs (black-and-white) were taken of particular features, as requested by individual scientists, for illustrations in the summary of each site. Video digital imaging was performed on some fine-scale features and is available from ODP upon request. The archive halves of cores from the second complete hole at each site (generally the "C" hole) were run through the cryogenic magnetometer prior to description and color analysis to provide those scientists sampling physical properties guidance in choosing sample intervals so as not to disturb significant magnetic reversal boundaries. The archive halves were then described visually, analyzed for light reflectance, and finally photographed.

The working half of the core was measured first for sonic velocity and vane shear strength. (During coring at the second complete hole at each site, these measurements were not performed until after the preliminary paleomagnetic data were available to avoid sampling intervals of paleomagnetic interest.) After physical properties sampling, the working half was sampled for reconnaissance-level and low-resolution shipboard and shore-based laboratory studies. Sampling for detailed high-resolution paleoceanographic and paleoclimatic studies was deferred until after the cruise to optimize the sampling with the stratigraphic information from biostratigraphy, paleomagnetic stratigraphy, and lithologic correlations.

Each sample taken was logged into the sampling data-base program by the location and the name of the investigator receiving the sample. Records of all of the samples removed are kept by the curator at ODP headquarters. The extracted samples were sealed in plastic vials or bags and labeled. Samples were routinely taken for shipboard physical property analysis. These samples were subsequently used for calcium carbonate (coulometric) and organic carbon (CNS elemental) analyses; these data are reported in the site chapters.

Both halves of the core were placed into labeled plastic tubes, which were then sealed and transferred to cold-storage space aboard the drilling vessel. At the end of the leg, the cores were transferred from the ship in refrigerated air-freight containers to cold storage at the Gulf Coast Repository of the Ocean Drilling Program, Texas A&M University, College Station, Texas.

LITHOSTRATIGRAPHY

Visual Core Description

Sediment "Barrel Sheets"

The core description forms (Fig. 3), or "barrel sheets," summarize the data obtained during shipboard analysis of each sediment core. The following discussion explains the ODP conventions used for compiling each part of the core description forms and the exceptions to these procedures adopted by the Leg 138 shipboard scientific party.

Shipboard sedimentologists were responsible for visual core logging, smear slide analyses, thin section descriptions of sedimentary and volcanoclastic material, and color analysis. Mineral composition data, determined by X-ray diffraction, were used in some cases to augment the visual core descriptions. Data describing biostratigraphy (age), geochemistry (CaCO₃, C_{org}, XRF), paleomagnetism, and physical properties (wet-bulk density and porosity) were integrated with sedimentological information.

In addition to the sedimentological information on the barrel sheets, plots of the GRAPE, magnetic susceptibility, and digital color reflectance spectroscopy data are displayed next to the traditional barrel sheet information (Fig. 3). The GRAPE and magnetic suscep-

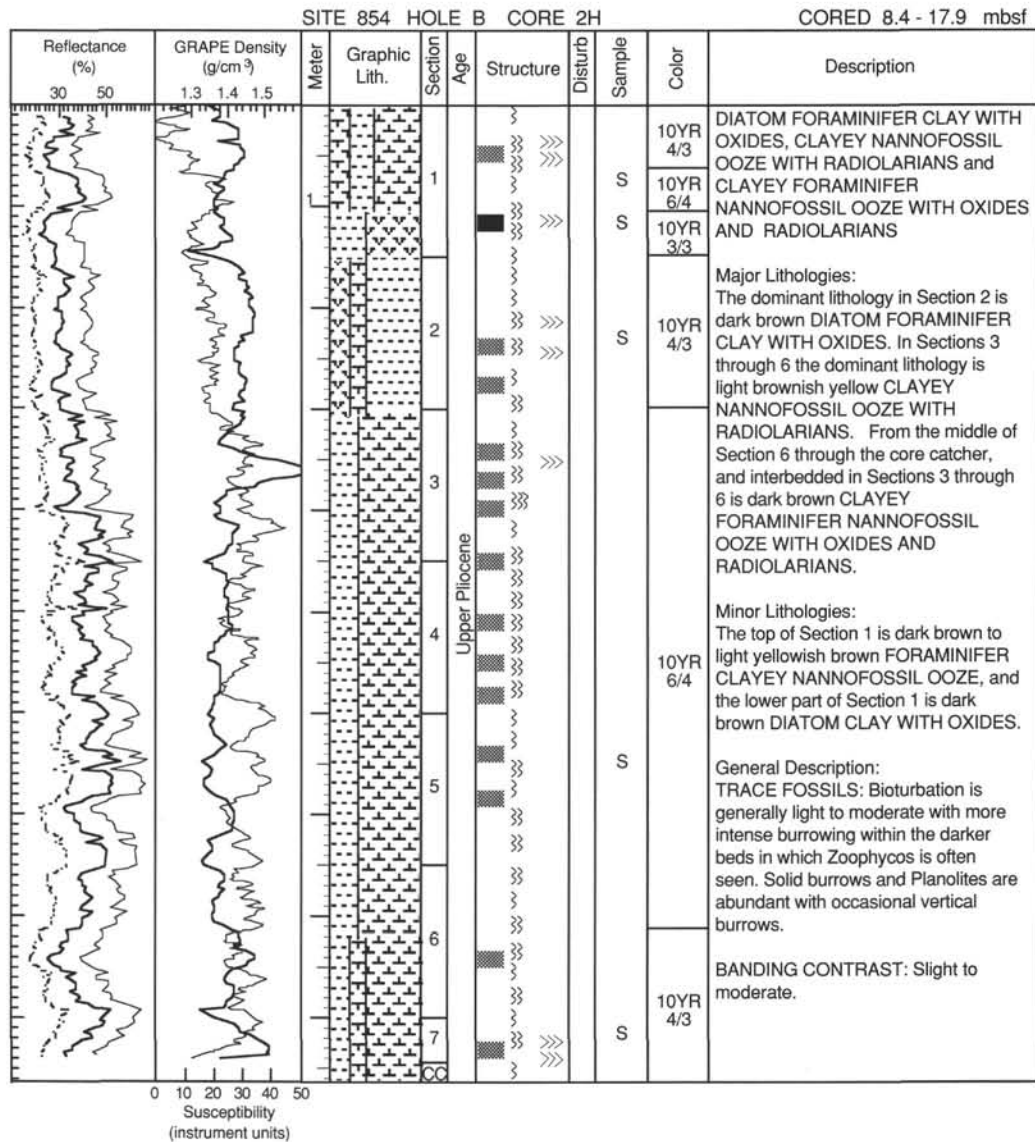


Figure 3. Example of a core description form ("barrel sheet") used for sediments and sedimentary rocks.

tibility data were available before the core was described, and sediments corresponding to specific features of these records were often examined in greater detail to determine their origin.

Core Designation

Cores are designated using leg, site, hole, core number, and core type as discussed in a preceding section (see "Numbering of Sites, Holes, Cores, and Samples" section, this chapter). The cored interval is specified in terms of meters below sea level (mbsl) and meters below seafloor (mbsf). On the basis of drill-pipe measurements (dpm), reported by the SEDCO coring technician and the ODP operations superintendent, depths are corrected for the height of the rig-floor dual elevator stool above sea level to give true water depth and correct meters below sea level.

Paleontological Data

The chronostratigraphic unit, as recognized on the basis of paleontological results, is shown in the "Age" column. Detailed explanations

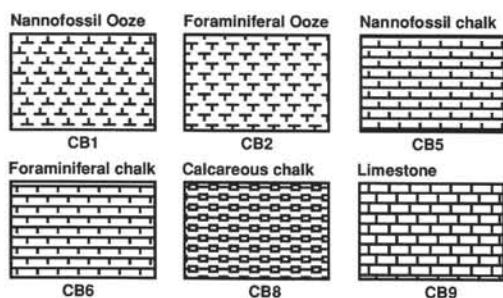
of the zonations used during Leg 138 are presented in the "Biostratigraphy" section (this chapter).

Graphic Lithology Column

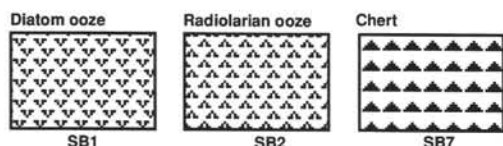
The lithology of the material recovered is represented on the core description forms by up to three symbols in the column titled "Graphic Lithology" (Figs. 3 and 4). Where an interval of sediment or sedimentary rock is a homogeneous mixture, the constituent categories have been separated by a solid vertical line, with each category represented by its own symbol. Constituents accounting for <10% of the sediment in a given lithology are not shown in the "Graphic Lithology" column but are listed in the "Lithologic Description" section of the barrel sheet. If more than three constituents are present in concentrations >10%, only the three most dominant constituents are shown graphically, in order of increasing abundance. However, all constituents present in amounts >10% are listed in the text description. In an interval comprising two or more sediment lithologies that have different compositions, such as in thin-bedded and highly variegated sediments, the average relative abundances of the lithologic con-

PELAGIC SEDIMENTS

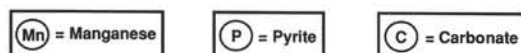
Calcareous



Siliceous

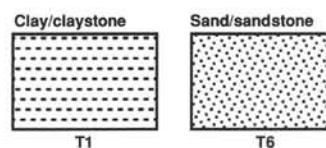


CONCRETIONS

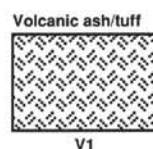


Drawn circle with symbol (others may be designated)

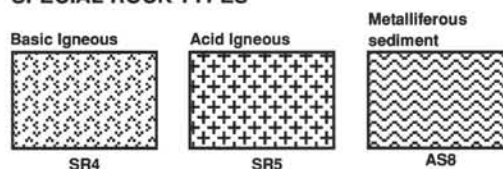
SILICICLASTIC SEDIMENTS



VOLCANICLASTIC SEDIMENTS



SPECIAL ROCK TYPES



MIXED SEDIMENTS

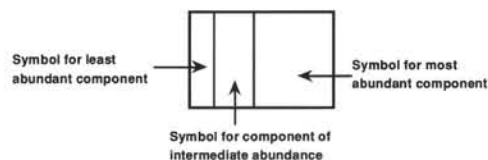


Figure 4. Key to symbols used in the "Graphic lithology" column on the core description form shown in Figure 3.

stituents are represented graphically by dashed lines that vertically divide the interval into appropriate fractions, as described above. The "Graphic Lithology" column shows only the composition of layers or intervals exceeding 20 cm in thickness. Video images of some finer-scale lithologic variations also were made. This information is available upon request from ODP.

Sedimentary Structures

In sediment cores, natural structures and structures created by the coring process can be difficult to distinguish. Natural structures observed are indicated in the "Structure" column of the core description form. The column is divided into three vertical areas for symbols (Fig. 5). The symbols on the left-hand side of the "Structure" column indicate the bedding characteristics (including color banding) of the sediment.

The intensity of bioturbation is shown in the central portion of the "Structure" column of the barrel sheet in the conventional manner (slight, moderate, heavy). In addition, the description section of each barrel sheet contains an additional heading, "Trace Fossils," which lists any trace fossils recognized in each core.

The symbols on the right side of the "Structure" column indicate the location of individual bedding features and any other sedimentary features, such as nodules, zeolite crystals, ash layers, and shell fragments. The symbols used to describe each of these primary and secondary biogenic and physical sedimentary structures are shown in Figure 6.

Sedimentary Disturbance

Sediment disturbance resulting from the coring process is illustrated in the "Disturbance" column on the core description form

(using symbols in Fig. 6). Blank regions indicate an absence of drilling disturbance. The degree of drilling disturbance is described for soft and firm sediments using the following categories:

1. Slightly deformed: bedding contacts are slightly bent.
2. Moderately deformed: bedding contacts have undergone extreme bowing.
3. Highly deformed: bedding is completely disturbed, sometimes showing symmetrical diapir-like or flow structures.
4. Soupy: intervals are water-saturated and have lost all aspects of original bedding.

The degree of fracturing in indurated sediments and igneous rocks is described using the following categories:

1. Slightly fractured: core pieces are in place and contain little drilling slurry or breccia;
2. Moderately fragmented: core pieces are in place or partly displaced, and original orientation is preserved or recognizable (drilling slurry may surround fragments);
3. Highly fragmented: core pieces are from the interval cored and probably in the correct stratigraphic sequence (although they may not represent the entire section), but original orientation is completely lost;
4. Drilling breccia: core pieces have lost their original orientation and stratigraphic position and may be mixed with drilling slurry.

Induration

The criteria used to determine the induration of pelagic sediments found during Leg 138 are subjective and provide three classes for pelagic oozes:

Key to barrel sheet "Structures" column

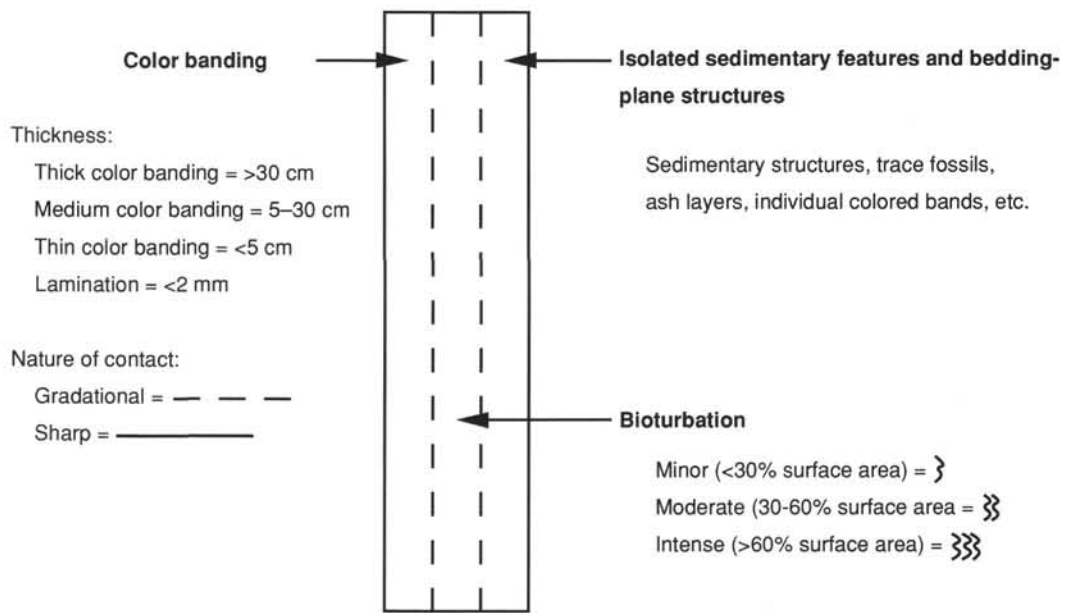


Figure 5. Layout of "Structures" column on the core description form shown in Figure 3.

1. Soft: sediments that have little strength and are readily deformed under the finger or broad blade of the spatula are termed oozes or clay;
2. Firm: partly lithified pelagic sediments as oozes or clays are readily deformed under the fingernail of the edge of a spatula blade;
3. Hard: nonfriable, cemented rocks.

The suffix "-stone" is added to the name of cemented rocks (e.g., limestone, claystone). Hard siliceous sedimentary rocks are called chert or porcellanite.

Color

The hue and chroma attributes of color were determined by comparison with Munsell soil-color charts as soon as possible after the cores were split because redox-associated color changes may occur when deep-sea sediments are exposed to the atmosphere. Information about Munsell core colors is given in the "Color" column on the core description form.

In addition to the traditional Munsell colors, the spectrum of colors reflected in the visible and near-infrared bands (450–950 nm) was determined digitally over 511 channels. The automated color analysis system used during Leg 138 was a prototype developed at Oregon State University and is described more fully in Mix et al. (this volume). The archive halves of all APC and most XCB cores were measured at intervals ranging from 1 to 8 cm using a computerized conveyor system similar to the ODP MST. To present some of this information on the barrel sheets, the 511 wavelengths measured were simplified to three bands, spanning the data sets: 450–500 nm ("blue"), 650–700 nm ("red"), and 850–900 nm ("near infrared"). These three bands were plotted as percentages of reflectance, adjacent to each barrel sheet. A dashed line represents the 450- to 500-nm wavelength; a bold solid line, the 650- to 700-nm wavelength; and a thin solid line, the 850- to 900-nm wavelength. Note that for Cores 138-845A-13H, -845B-18H, -19H, and -21H, the 650 to 700 nm wavelength is

represented by a thin solid line and the 850 to 900 nm wavelength is represented by a bold solid line.

Samples

The position of samples taken from each core for shipboard analysis is indicated in the "Samples" column on the core-description form (Fig. 3). The symbol "S" indicates the location of smear-slide samples, the symbol "T" indicates the location of thin-section samples, and the symbol "M" indicates the location of paleontology samples. The notations "I" and "P" designate the location of samples for whole-round interstitial-water geochemistry and physical property analyses, respectively.

Smear Slide Summary

A figure summarizing the major component data determined from smear slides appears in each site chapter, and a table summarizing data from smear slide and thin section analyses appears at the end of each site chapter. This table includes information about the sample location, whether the sample represents a dominant ("D") or a minor ("M") lithology in the core, and the estimated percentages of sand, silt, and clay, together with all identified components. In many cored intervals, the lithology is highly variable on scales of 10 cm to 10 m. Our use of the "minor" lithology designation for smear slides evolved over the leg. In describing smear slides from Sites 844 through 846, the "minor" designator was used for any lithology that did not represent more than 30% of a single core. We found that this restriction masked the importance of beds and interbeds that were characteristic of specific lithologic intervals in our smear slide summaries. When describing smear slides from Sites 847 through 854, the "minor" designator was generally used for incidental or exotic lithologies (e.g., burrow fills, ash pods, etc.). Note that smear slide analyses tend to underestimate the abundance of foraminifers and volcanoclastic-detri-

Drilling disturbance symbols

Soft sediments	
	Slightly disturbed
	Moderately disturbed
	Highly disturbed
	Soupy
Hard sediments	
	Slightly fractured
	Moderately fractured
	Highly fragmented
	Drilling breccia

Sedimentary structures

	Interval over which primary sedimentary structures occur
	Fining-upward sequence
	Coarsening-upward sequence
	Reduction of particle abundance
	Planar laminae
	Wedge-planar laminae/beds
	Graded bedding (normal)
	Graded bedding (reversed)
	Scoured contact with graded beds
	Sharp contact
	Gradational contact
	Scoured, sharp contact
	Thick color bands (sharp contact)
	Thick color bands (gradational contact)
	Medium color bands (sharp contact)
	Medium color bands (gradational contact)
	Thin color bands (sharp contact)
	Thin color bands (gradational contact)
	Laminations (mm scale)
	Individual thick color band
	Individual medium color band
	Individual thin color band
	Individual lamination
	Carbonate nodule
	Chert nodule
	Manganese nodule
	Disseminated manganese
	Pyrite nodule
	Disseminated pyrite
	Zeolite

	Load casts
	Slump blocks or slump folds
	Contorted Slump
	Scour
	Imbrication
	Clastic dike
	Veins
	Ash or pumice pods
	Ash layer
	Micro fault (normal)
	Micro fault (thrust)
	Macro fault
	Fracture
	Mineral-filled fracture
	Injection
	Probable compaction fracture
	Tension gashes
	Vugs
	Bioturbation, minor (<30% surface area)
	Bioturbation, moderate (30%—60% surface area)
	Bioturbation, strong (>60% surface area)
	Discrete <i>Zoophycos</i> trace fossil
	Fossils, general (megafossils)

Figure 6. Symbols used for drilling disturbance and sedimentary structure on the core description form shown in Figure 3.

tal material because these larger grains are difficult to incorporate into the smear.

tions and locations of thin, interbedded, or minor lithologies are included in the text.

Lithologic Description—Text

The lithologic description that appears on each core description form (barrel sheet) consists of three parts: (1) a heading that lists all the major sediment lithologies (see "Sedimentology" section, this chapter) observed in the core; (2) a heading for minor lithologies, and (3) a more detailed description of these sediments, including location in the core of significant features, a census of trace fossils, and a subjective index of the contrast in color banding in the core. Descrip-

Sedimentology

The sediments recovered from the equatorial Pacific Ocean during Leg 138 are primarily biogenous. The region is remote from terrestrial sources of clastic sediment and from shallow areas supplying neritic sediments, and the sediments contain only a few thin ash layers. Therefore, we chose not to use the ODP granular sediment classification scheme formulated by Mazzullo et al. (1987). Instead, we used a combination of the classification scheme for biogenous sediments (Fig. 7) developed for

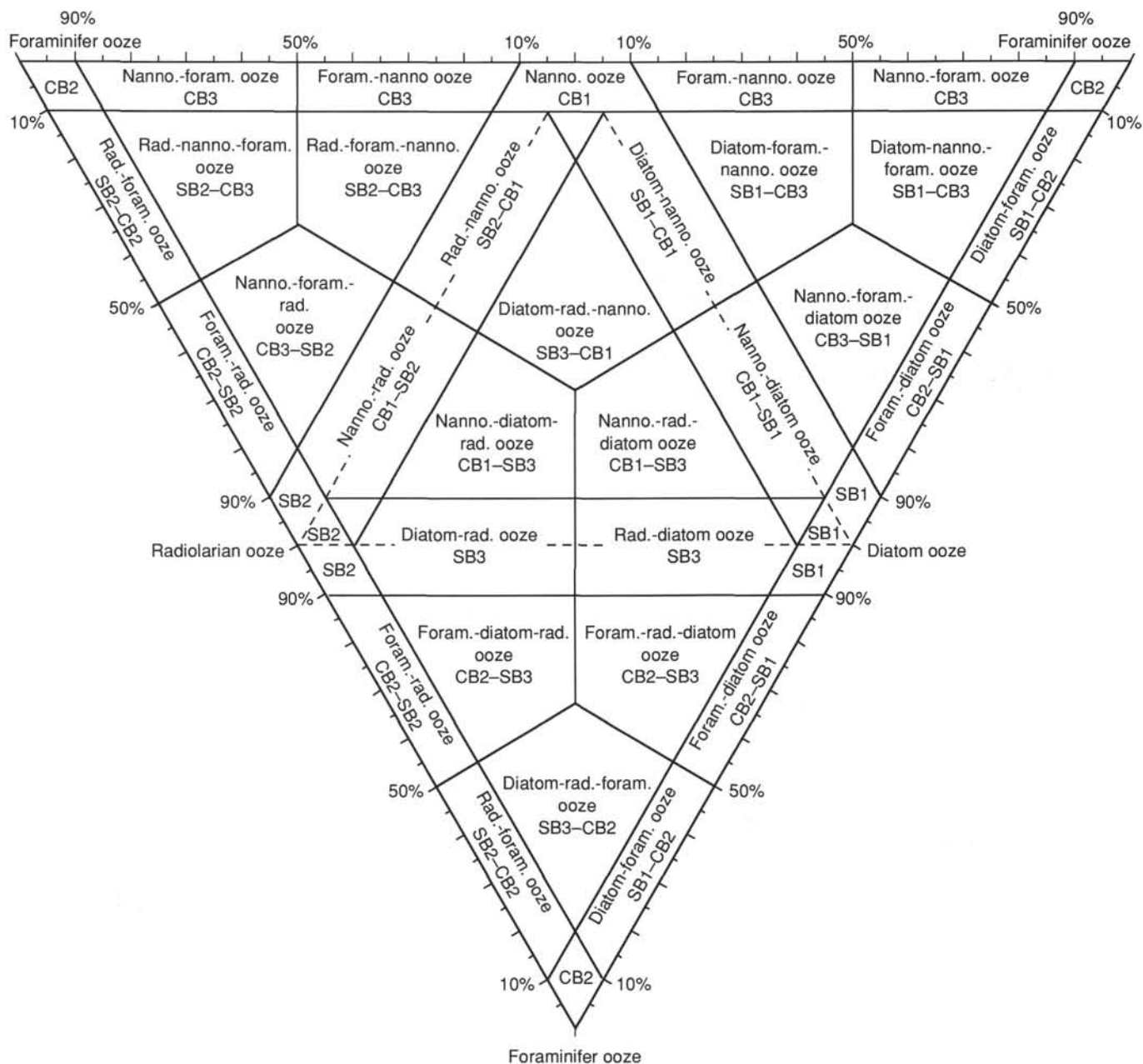


Figure 7. Diagram showing classes of biogenic sediment (modified from Shipboard Scientific Party, 1985).

an earlier equatorial Pacific drilling leg (Leg 85 Shipboard Scientific Party, 1985) and the portion of the ODP classification scheme (Mazzullo et al., 1987) applicable to siliciclastic sediments.

Granular Sediments

Fine-grained biogenic sediments are composed of the fine-grained skeletal debris of open-marine siliceous and calcareous microfauna and microflora (e.g., radiolarians, calcareous nannofossils) and associated organisms. Siliciclastic grains are composed of mineral and rock fragments that were derived from igneous, sedimentary, and metamorphic rocks. Variations in the relative proportions of the two sediment types, biogenous and siliciclastic, define the major classes of granular sediments, as follows:

1. Biogenic sediments are composed of >50% biogenic grains and <50% siliciclastic grains.
2. Siliciclastic sediments are composed of >50% siliciclastic grains and <50% biogenic grains.

Classification of Granular Sediment

A granular sediment may be classified by designating a principal name and major and minor modifiers. The principal name of a granular sediment defines its granular sediment class; the major and minor modifiers describe the texture, composition, fabric, and/or shape of the grains themselves (Table 1).

Principal Names

Each granular sediment class has a unique set of principal names, which are outlined in Table 1.

For biogenic sediment, the principal name describes the composition and degree of consolidation using the following terms:

1. Ooze: unconsolidated calcareous and/or siliceous biogenic sediments.
2. Chalk: firm biogenic sediment composed predominantly of calcareous biogenic grains.
3. Chert: vitreous or lustrous, conchoidally fractured, highly indurated rock composed predominantly of redeposited silica.

For siliciclastic sediment, the principal name describes the texture and is assigned according to the following guidelines:

1. The Udden-Wentworth grain-size scale (Wentworth, 1922; Table 2) defines the grain-size ranges and the names of the textural groups (gravel, sand, silt, and clay) and subgroups (fine sand, coarse silt, etc.) that are used as the principal names of siliciclastic sediment.
2. When two or more textural groups or subgroups are present in a siliciclastic sediment, they are listed as principal names in order of increasing abundance.
3. The suffix "stone" is affixed to the principal names sand, silt, and clay when the sediment is lithified. Conglomerate and breccia are used as principal names of gravels having well-rounded and angular clasts, respectively.

The only volcanoclastic sediment encountered in the sediments recovered during Leg 138 was volcanic ash. Volcanic ash consists of pyroclasts <2 mm in diameter. If this material is lithified, the term "tuff" is used.

Major and Minor Modifiers

The principal name of a granular sediment class is preceded by major modifiers and is followed by minor modifiers (preceded by the term "with") that describe the lithology of the granular sediment in

Table 1. Outline of sediment classification scheme (modified from Shipboard Scientific Party, 1985).

Sediment class	Major modifier	Principal names	Minor modifiers
Biogenic	1. Composition of biogenic and neritic grains present in major amounts. 2. Texture of clastic grains present in major amounts.	1. Ooze 2. Chalk 3. Limestone 4. Radiolarite 5. Diatomite 6. Spiculite 7. Chert	1. Composition of biogenic grains present in minor amounts.
			2. Texture of clastic grains present in minor amounts.
Siliciclastic	1. Composition of all grains present in major amounts. 2. Grain fabric (gravels only) 3. Grain shape (optional) 4. Sediment color (optional)	1. Gravel 2. Sand 3. Silt 4. Clay (etc.)	1. Composition of all grains present in minor amounts.
			2. Texture and composition of siliciclastic grains present as matrix (for coarse-grained clastic sediment).
Volcanoclastic	1. Composition of all volcanoclasts present in major amounts. 2. Composition of all pelagic grains present in major amounts. 3. Texture of siliciclastic grains present in major amounts.	1. Breccia 2. Lapilli 3. Ash/tuff	1. Composition of all volcanoclasts present in minor amounts.
			2. Composition of all pelagic grains present in minor amounts.
			3. Texture of siliciclastic grains present in minor amounts.

Table 2. Udden-Wentworth grain-size scale for siliciclastic sediments (Wentworth, 1922).

Millimeters	Micrometers	Phi (φ)	Wentworth size class	
		-20		Gravel
		-12	Boulder (-8 to -12φ)	
		-10		
		-8		
		-6	Cobble (-6 to -8φ)	
		-4	Pebble (-2 to -6φ)	
		-2		Sand
		-1.75		
		-1.5	Granule	
		-1.25		
		-1.0		
		-0.75		
		-0.5	Very coarse sand	
		-0.25		
		0.0		
		0.25	Coarse sand	
		0.5		
		0.75		
1/2	500	1.0		
	420	1.25	Medium sand	
	350	1.5		
	300	1.75		
1/4	250	2.0		
	210	2.25	Fine sand	
	177	2.5		
	149	2.75		
	125	3.0		
1/8	106	3.25		
	88	3.5	Very fine sand	
	74	3.75		
1/16	63	4.0		
	53	4.25		
	44	4.5	Coarse silt	
	37	4.75		
1/32	31	5.0		
1/64	15.6	6.0	Medium silt	
1/128	7.8	7.0	Fine silt	
1/256	3.9	8.0	Very fine silt	
	2.0	9.0		
	0.96	10.0	Clay	
	0.49	11.0		
	0.24	12.0		
	0.12	13.0		
	0.06	14.0		
				Mud

greater detail (Table 1). The most common use of major and minor modifiers is to describe the composition and textures of grain types that are present in major (>10%) and minor (<10%) proportions. Note that major modifiers are always listed in order of increasing abundance. Thus, a diatom-foraminifer-nannofossil ooze contains more nannofossils than foraminifers and more foraminifers than diatoms.

The modifiers for biogenic sediments and the percentages of each sediment type to which they apply are shown in Figure 7. This modifier scheme is the same as that used for equatorial Pacific Ocean sediments recovered during DSDP Leg 85 (Shipboard Scientific Party, 1985). The texture of siliciclastic grains is described by the major and minor modifiers gravel(-ly), sand(-y), silt(-y), and clay(-ey). The composition of siliciclastic grains can be described by:

1. Mineralogy: using modifiers such as "quartz," "pyrite," "zeolitic" (for rock fragments) and "calcareous" (for detrital clasts of calcium carbonate).

2. Provenance: the source of rock fragments (particularly in gravels, conglomerates, and breccias) can be described by modifiers such as volcanic, sed-lithic, meta-lithic, gneissic, basaltic, etc.

The composition of volcanoclastic grains is described by the major and minor modifiers lithic (rock fragments), vitric (glass and pumice), and crystal (mineral crystals), or by modifiers that describe the compositions of the lithic grains and crystals (e.g., feldspar or basaltic). The fabric of the sediment can be described by the major modifiers, grain-supported, matrix-supported, and imbricated. Generally, fabric descriptors are applied only to gravels, conglomerates, and breccias, for they provide useful information on their transport history.

Chemical Sediments

Classes of Chemical Sediments

Chemical sediments are composed of minerals that formed by inorganic processes, such as precipitation from solution or colloidal suspension, deposition of insoluble precipitates, or recrystallization of siliceous, calcareous, or carbonaceous (plant) debris. They often have a crystalline (i.e., nongranular) texture. Three types of chemical sediments were found in the sediments of Leg 138: silicates, carbonates, and metalliferous sediments and related oxides. Each class of chemical sediment has its own distinctive classification scheme.

Silicates and Carbonates

Silicates and carbonates are defined as sedimentary rocks that are nongranular and nonbiogenic in appearance and are composed of silicate and carbonate minerals. Silicates and carbonates may have formed from the recrystallization of siliceous and calcareous grains, but they are distinguished by the absence of clearly identifiable granular and/or biogenic components. They may form as primary precipitates or as hydrothermal alteration products. Zeolites may form in either of these two ways. The chemical sediment types are classified according to their mineralogy, using principal names such as calcite or dolomite. Because the XRD unit was inoperative after Site 847, we were unable to specify the mineralogy of some chemical sediments found in later sites. They should also be modified with terms that describe their crystalline (as opposed to granular) nature, such as crystalline, microcrystalline, massive, and amorphous.

Metalliferous Sediments and Metal-Rich Oxides

Metalliferous sediments are composed of fine-grained granular oxides and hydroxy oxides rich in iron and other transition elements.

They may occur near or within basement rocks in the sedimentary section or as dispersed grains as a minor component of other sediments. In the former instance, the metal-rich sediments may include both primary precipitates and altered crystalline phases. They may also include x-ray amorphous semi-opaque oxides.

Metalliferous sediments are generally distinguished from other fine-grained nonbiogenic sediments on the basis of their chemistry (e.g., Fe ≥ 10 wt% on a carbonate-free basis; {[Fe + Mn]/Ti} ≥ 25). In the absence of such information at the time the cores were described, we distinguished this sediment lithology on the basis of color, oxide content of smear slides, and/or occurrence at the base of the sediment column.

Other metal-rich oxides, such as dispersed or nodular manganese oxides, also occur in equatorial Pacific sediments. They may occur near the sediment surface or may lie buried within the sediment. They are distinguished by color, mineralogy, and, in the case of nodules, by their physical appearance.

BIOSTRATIGRAPHY

Time Scale/Chronological Framework

During Leg 138, we adhered in part to the geomagnetic polarity time scale (GPTS) of Berggren et al. (1985) to provide correlation between the magnetostratigraphy and the chronological scale (Table 3, Fig. 8). This time scale has been modified to incorporate the Blake, Cobb Mountain, and Reunion paleomagnetic events (Table 3). Calibration of the biostratigraphy to this time scale (Fig. 9) is similar to that used during Leg 130 (Kroenke, Berger, Janecek, et al., 1991). For calcareous nannofossil biostratigraphy, this reflects improved calibration between calcareous nannofossil events and the geopolarity time scale (Leg 115; Backman et al., 1990; Olafsson, 1991). However, several calcareous nannofossil events have been recalibrated on the basis of Leg 138 cruise results (Table 4). Calibration of the foraminifers and radiolarian biochronology follows that of Berggren et al. (1985). Calibration of diatom biochronology follows that of Barron (1985b; in press). In Tables 4 and 5, we show the magnetic calibration and the estimated ages of biostratigraphic datums used during Leg 138.

Age assignments of the standard epoch boundaries are as follows:

Epoch	Age (Ma)	Reference
Pleistocene/Pliocene	1.66	Tauxe et al. (1983)
late Pliocene/early Pliocene	3.4	Berggren et al. (1985)
Pliocene/Miocene	4.9/5.3	Berggren et al. (1985) and Zijderveld et al. (1986)
^a late/middle Miocene	10.6	Berggren et al. (1985)
middle/early Miocene	16.0	Berggren et al. (1985)
Miocene/Oligocene	23.7	Berggren et al. (1985)

^aAlthough we adhere throughout this report to the placement of the late/middle boundary according to Berggren et al. (1985), one should note that Rio et al. (1990a) propose reassignment of this boundary based on reevaluation of the microfossils from the Tortonian stratotype. The co-occurrence of *Neogloboquadrina acostaensis* and *Discoaster hamatus* suggests that the first occurrence of *N. acostaensis* does not represent the true first occurrence of *N. acostaensis* and that the base of the Tortonian lies in the upper part of Zones CN7/NN9.

Biostratigraphy

Preliminary age assignments are based on biostratigraphic analysis of calcareous nannofossils, foraminifers, radiolarians, and diatoms. Stratigraphic constraint of calcareous nannofossil and diatom datums are based on examining one to four samples per stratigraphic section

Table 3. Neogene geomagnetic polarity time scale and magnetostratigraphic nomenclature used during Leg 138.

Chron/subchron/event	Sense	Age (Ma)	Anomaly
Blake	Midpoint	0.11	1
Brunhes/Matuyama	R->N	0.73	
Jaramillo(t)	N->R	0.91	
Jaramillo(o)	R->N	0.98	
Cobb Mountain	Midpoint	*1.10	
Olduvai(t)	N->R	1.66	
Olduvai(o)	R->N	1.88	2
Réunion(t)	N->R	*2.06	
Réunion(o)	R->N	*2.09	
Matuyama/Gauss	N->R	2.47	
Kaena(t)	R->N	2.92	2A
Kaena(o)	N->R	2.99	
Mammoth(t)	R->N	3.08	2A
Mammoth(o)	N->R	3.18	
Gauss/Gilbert	R->N	3.40	2A
Cochiti(t)	N->R	3.88	
Cochiti(o)	R->N	3.97	3
Nunivak(t)	N->R	4.10	
Nunivak(o)	R->N	4.24	3
Sidjufall(t)	N->R	4.40	
Sidjufall(o)	R->N	4.47	3
Thvera(t)	N->R	4.57	
Thvera(o)	R->N	4.77	3
C3A-n1(t)	N->R	5.35	
C3A-n1(o)	R->N	5.53	3A
C3A-n2(t)	N->R	5.68	
C3A-n2(o)	R->N	5.89	3A
C3A-n3(t)	N->R	6.37	
C3A-n3(o)	R->N	6.50	
C4-n1(t)	N->R	6.70	
C4-n1(o)	R->N	6.78	4
C4-n2(t)	N->R	6.85	
C4-n2(o)	R->N	7.28	4
C4-n3(t)	N->R	7.35	
C4-n3(o)	R->N	7.41	4
C4A-n1(t)	N->R	7.90	
C4A-n1(o)	R->N	8.21	4A
C4A-n2(t)	N->R	8.41	
C4A-n2(o)	R->N	8.50	4A
C4A-n3(t)	N->R	8.71	
C4A-n3(o)	R->N	8.80	
C5-n1(t)	N->R	8.92	
C5-n1(o)	R->N	10.42	5
C5-n2(t)	N->R	10.54	
C5-n2(o)	R->N	10.59	
C5-n3(t)	N->R	11.03	
C5-n3(o)	R->N	11.09	
C5A-n1(t)	N->R	11.55	
C5A-n1(o)	R->N	11.73	5A
C5A-n2(t)	N->R	11.86	
C5A-n2(o)	R->N	12.12	5A
C5A-n3(t)	N->R	12.46	
C5A-n3(o)	R->N	12.49	
C5A-n4(t)	N->R	12.58	
C5A-n4(o)	R->N	12.62	
C5AA-n(t)	N->R	12.83	
C5AA-n(o)	R->N	13.01	5AA
C5AB-n(t)	N->R	13.20	
C5AB-n(o)	R->N	13.46	5AB
C5AC-n(t)	N->R	13.69	
C5AC-n(o)	R->N	14.08	5AC
C5AD-n(t)	N->R	14.20	
C5AD-n(o)	R->N	14.66	5AD
C5B-n1(t)	N->R	14.87	
C5B-n1(o)	R->N	14.96	5B
C5B-n2(t)	N->R	15.13	
C5B-n2(o)	R->N	15.27	5B
C5C-n1(t)	N->R	16.22	
C5C-n1(o)	R->N	16.52	5C
C5C-n2(t)	N->R	16.56	
C5C-n2(o)	R->N	16.73	5C
C5C-n3(t)	N->R	16.80	
C5C-n3(o)	R->N	16.98	5C
C5D-n1(t)	N->R	17.57	
C5D-n1(o)	R->N	17.90	5D
C5D-n2(t)	N->R	18.12	
C5D-n2(o)	R->N	18.14	5D
C5E-n(t)	N->R	18.56	
C5E-n(o)	R->N	19.09	5E
C6-n(t)	N->R	19.35	
C6-n(o)	R->N	20.45	6
C6A(t)	N->R	20.88	
C6A(o)	R->N	21.16	6A
C6A(t)	N->R	21.38	
C6A(o)	R->N	21.71	6A
C6AA(t)	N->R	21.90	
C6AA(o)	R->N	22.06	6AA
C6AA(t)	N->R	22.25	
C6AA(o)	R->N	22.35	6AA
C6B(t)	N->R	22.57	
C6B(o)	R->N	22.97	6B
C6C(t)	N->R	23.27	
C6C(o)	R->N	23.44	6C
C6C(t)	N->R	23.55	
C6C(o)	R->N	23.79	6C
C6C(t)	N->R	24.04	
C6C(o)	R->N	24.21	6C

Notes: The magnetic polarity time scale generally follows Berggren et al. (1985). t = termination; o = origin; R = reverse polarity; N = normal polarity.
 *Age from Mankinen and Dalrymple (1979).

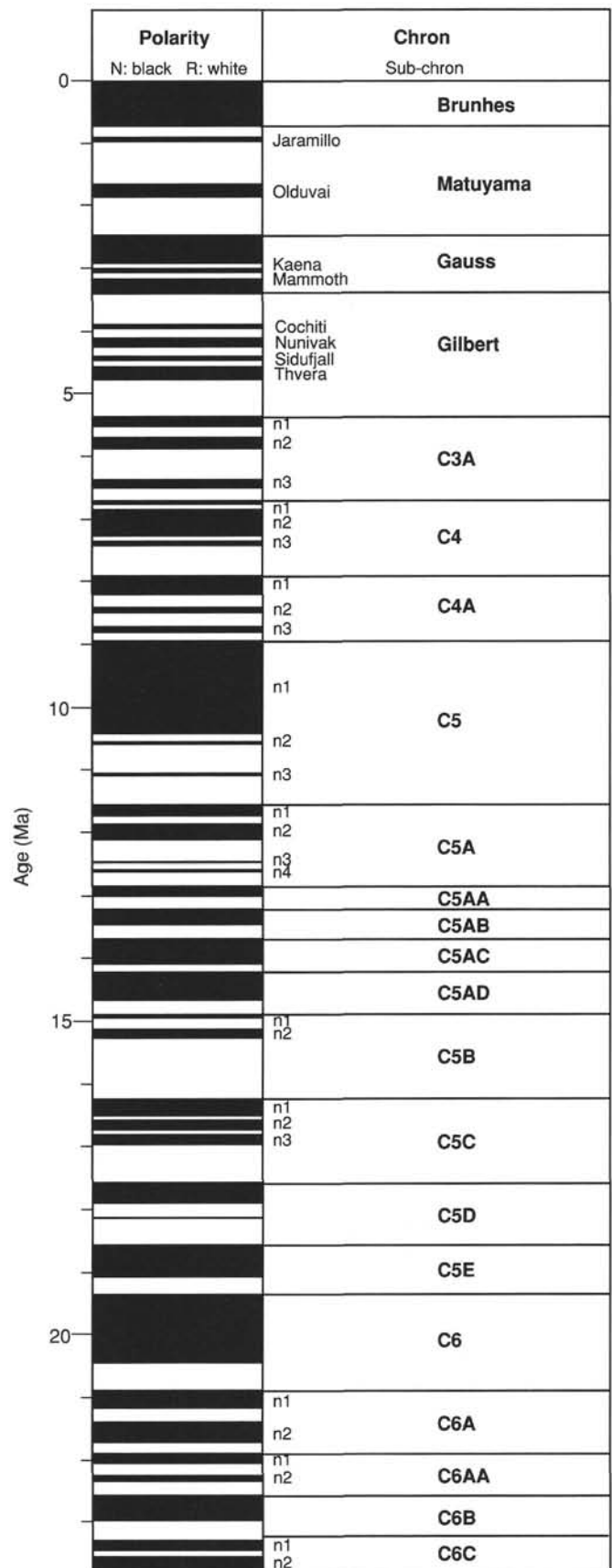


Figure 8. Neogene geomagnetic polarity time scale and magnetostratigraphic nomenclature used during Leg 138. The magnetic polarity time scale follows

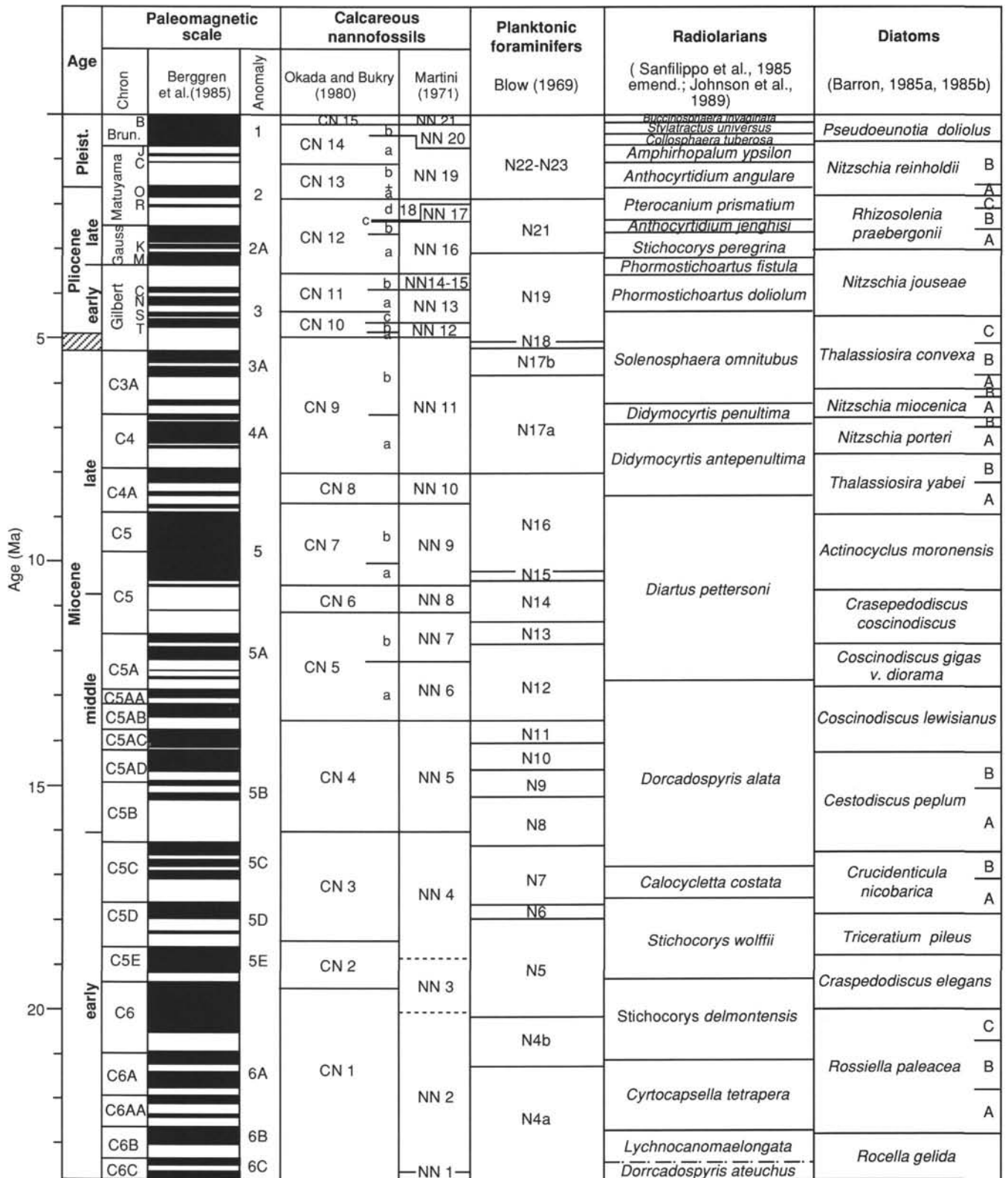


Figure 9. Correlation of the Neogene chronostratigraphy, biostratigraphy, and magnetostratigraphy used during Leg 130. Correlation of the magnetic polarity record and the epoch boundaries follows that of Berggren et al. (1985). Data on the calibration of zonal indicators with magnetostratigraphy can be found in Tables 4 and 5. Calcareous nannofossil biochronology follows Backman et al. (1990); foraminifer and radiolarian biochronology follows Berggren et al. (1985); and diatom biochronology follows Barron (1985a, 1985b). The hatched area at the Miocene/Pliocene boundary shows that the range in age of the boundary is between 5.3 (Berggren et al., 1985) and 4.9 Ma (Zijderveld et al., 1986).

Table 4. Magnetic calibration and the estimated ages of Neogene calcareous nannofossil events used during Leg 138 based on the paleomagnetic time scale of Berggren et al.

Event	Calibration	Age (Ma)	Zone (base)
T <i>Emiliana huxleyi</i>		0.085 (1)	
B <i>Emiliana huxleyi</i>		0.26 (1)	CN15/NN21
T <i>Pseudoemiliana lacunosa</i>		0.461 (1)	CN14b/NN20
B <i>Gephyrocapsa</i> sp.3	Jaramillo	0.92 (2)	
T <i>Gephyrocapsa</i> spp. >5.5 μm		1.12 (2)	~CN14a
B <i>Gephyrocapsa</i> spp. >5.5 μm		1.32 (2)	
T <i>Calcidiscus macintyreii</i>		1.45 (3)	
B <i>Gephyrocapsa oceanica</i> s.l.		1.58 (2)	
T <i>Discoaster brouweri</i>	Olduvai	1.89 (3)	CN13a/NN19
BA <i>Discoaster triradiatus</i>		2.07 (9)	
T <i>Discoaster pentaradiatus</i>	Matuyama	2.35 (3)	CN12d/NN18
T <i>Discoaster surculus</i>		2.41 (3)	CN12c/NN17
T <i>Discoaster tamalis</i>	Gauss	2.65 (3)	CN12b
T <i>Sphenolithus</i> spp.	Gilbert	3.45 (3)	
T <i>Reticulofenestra pseudoumbilicus</i>	Gilbert	3.56 (3)	CN12a/NN16
BC <i>Discoaster asymmetricus</i>	Gilbert	3.83 (4)	CN11b
T <i>Amaurolithus primus</i>		4.37 (5)	CN11a
T <i>Ceratolithus acutus</i>	Sidufjall	4.43 (5)	
B <i>Ceratolithus rugosus</i>	Thvera	4.66 (5)	CN10c/NN13
B <i>Ceratolithus acutus</i>	Gilbert	4.85 (5)	CN10b
B <i>Triquetrorhabdulus rugosus</i>	Gilbert	4.90 (6)	CN10b
T <i>Discoaster quinqueramus</i>	Gilbert	4.98 (6)	CN10a/NN12
T <i>Amaurolithus amplifiscus</i>	C3A	5.33 (5)	
B <i>Amaurolithus amplifiscus</i>	C3A	6.02 (5)	
B <i>Amaurolithus primus</i>	C3A/C4	6.70 (5); 6.42(10)	CN9b/NN11
B <i>Discoaster quinqueramus</i>	C4	7.46 (6)	
B <i>Discoaster berggreni</i>	C4	8.00 (5); 7.5(11)	CN9a/NN11
B <i>Mnylitha conwallis</i>	C4A	(5)	CN8a/NN10
T <i>Discoaster hamatus</i>	C4A	8.67 (6)	CN8a/NN10
T <i>Catinaster</i> spp.	C4A	8.77 (6)	
B <i>Discoaster neohamatus</i>	C5	8.96 (6)	
B <i>Catinaster calyculus</i>	C5	10.0 (7)	
T <i>Coccolithus miopelagicus</i>	C5	10.4 (8); 9.94 (11)	
B <i>Discoaster hamatus</i>	C5	10.5 (6)	CN7a/NN9
B <i>Catinaster coalitus</i>		11.1 (6)	CN6/NN8
T <i>Cyclicargolithus floridanus</i>		11.5 (8)	
B <i>Discoaster kugleri</i>	C5A	12.2 (6)	CN5b/NN7
B <i>Calcidiscus macintyreii</i>			
B <i>Triquetrorhabdulus rugosus</i>	C5A	12.5 (8)	
B <i>Reticulofenestra pseudoumbilicus</i>	C5A	12.7 (8)	
T <i>Coronocyclus nitescens</i>	~C5A/C5AA	12.8 (5)	
TC <i>Cyclicargolithus floridanus</i>	C5AA	13.1 (6)	CN5a/NN6
T <i>Sphenolithus heteromorphus</i>	C5AB	13.5 (8)	CN5a/NN6
T <i>Helicosphaera ampliapertura</i>	C5B	16.00 (5)	CN4/NN5
TA <i>Discoaster deflandrei</i>	C5B	16.05 (5)	
B <i>Discoaster signus</i>	C5B	16.05 (5)	
B <i>Sphenolithus heteromorphus</i>	C5D	18.42 (6)	CN3
T <i>Sphenolithus belemnus</i>	C5E	18.8 (6)	NN4
B <i>Sphenolithus belemnus</i>	C6	19.46 (8)	CN2
T <i>Triquetrorhabdulus carinatus</i>		19.5(6)/23.0(8)	NN3
B <i>Discoaster druggi</i>	C6C	23.6 (6)	CN1c/NN2
TA <i>Sphenolithus delphix</i>		23.6 (7)	
T <i>Discoaster bisectus</i>		23.8 (8)	
A <i>Sphenolithus delphix</i>		24.7 (7)	
T <i>Sphenolithus cipoensis</i>	C6C/C7	25.2 (6)	CN1a

Notes: T=top; B=bottom; TA=top acme; BA=bottom acme; BC=bottom common occurrence; TC=top common occurrence. Number in parentheses indicates reference to calibration; 1=Thierstein et al. (1977); 2=Rio et al. (in press); 3=Backman and Shackleton (1983); 4=Rio et al. (1990a); 5=Rio et al. (1990b); 6=Backman et al. (1990); 7=Fornaciari et al. (1990); 8=Olafsson (1991); 9=Backman and Pestiaux (1986); 10=recalibration based on Leg 138 results from Site 848 (see "Sedimentation Rate" section, this chapter); 11=recalibration based on Leg 138 results from Site 845 (see "Sedimentation Rate" section, this chapter).

(0.5- to 1.5-m intervals). Constraint of foraminifer and radiolarian datums are based on examining one to three samples per core. The abundance, preservation, and zonal assignment for each sample is recorded in the stratigraphic site summary sheets.

Calcareous Nannofossils

During Leg 138, we referred to the zonal schemes proposed by Martini (1971) and Bukry (1973, 1975), code numbered by Okada and Bukry (1980). These zonations are regarded as "standard" for the biostratigraphic classification of Cenozoic marine sediments based on calcareous nannofossils. Modifications to these standard zonations and identification of new marker species have been proposed to improve the chronostratigraphic resolution for the Pleistocene (Gartner, 1977). We incorporate several of these newly proposed datums into the Leg 138 stratigraphic framework.

In Table 4, we have listed primary biostratigraphic events (zonal indicators) and secondary biostratigraphic events for the Miocene

through Holocene. The age assignments listed in Table 4 are taken from Backman et al. (1990), Rio et al. (in press), Rio et al. (1990a, 1990b), and Olafsson (1991). Most of the events have been tied directly to magnetostratigraphic records, although not all are unambiguous.

Methods

The nannofossil assemblages were described from smear slides prepared from unprocessed material. The slides were examined with a light microscope at about 1250× magnification using cross-polarized and transmitted light. Abundances of nannofossils in the slides were estimated for optimum density areas of the slides; that is, areas where most of the field was covered by sample material without appreciable piling of specimens or sample material. Abundances of the index species were estimated by means of the following procedures:

1. To characterize the general makeup of the assemblage, the first 100–200 specimens, encountered under a light microscope using

Table 5. Magnetic calibration and the estimated ages of Neogene diatom events used during Leg 138 based on the paleomagnetic time scale of Berggren et al. (1985).

Event	Calibration	Age (Ma)	Zone (base)
T <i>Nitzschia reinholdii</i>	Brunhes	0.65 (1)	<i>P. doliolus</i>
T <i>Nitzschia fossilis</i>		0.85	
T <i>Rhizosolenia matuyama</i>	Jaramillo	0.94 (2)	
B <i>Rhizosolenia matuyama</i>		1.1 (2)	
T <i>Rhizosolenia praebergonii</i> var. <i>robusta</i>	Matuyama	1.55 (1)	A/B boundary
B <i>Pseudoeunotia doliolus</i>	Olduvai	1.8 (2)	<i>N. reinholdii</i>
T <i>Rhizosolenia praebergonii</i>	Olduvai	1.85 (2)	
T <i>Thalassiosira convexa</i>	Matuyama	2.1 (1)	B/C boundary
T <i>Nitzschia jouseae</i>	Gauss	2.6 (1)	A/B boundary
B <i>Rhizosolenia praebergonii</i>	Gauss	3.0 (1)	<i>R. praebergonii</i>
T <i>Actinocyclus ellipticus</i> f. <i>lanceolata</i>		3.2	
B <i>Thalassiosira convexa</i> var. <i>convexa</i>	Gilbert	3.6 (3)	
B <i>Asteromphalus elegans</i>	Gilbert	3.9 (2)	
T <i>Nitzschia cylindrica</i>	Gilbert	4.3 (2)	
B <i>Nitzschia jouseae</i>	Gilbert	4.5 (2)	<i>N. jouseae</i>
B <i>Thalassiosira oestrupii</i>	Gilbert	5.1 (2)	
T <i>Thalassiosira miocenica</i>	Gilbert	5.1 (2)	B/C boundary
T <i>Asterolampra acutiloba</i>	C3A-n1	5.35 (2)	
T <i>Nitzschia miocenica</i>	C3A-n1	5.55 (2)	
T <i>Nitzschia miocenica</i> var. <i>elongata</i>	C3A-n1	5.65 (2)	
T <i>Thalassiosira praeconvexa</i>	C3A-n2	5.8 (2)	A/B boundary
T <i>Rossiella praepaleacea</i>	C3A-n2	6.0 (2)	
B <i>Thalassiosira miocenica</i>	C3A-n2	6.1 (2)	
B <i>Thalassiosira convexa</i>	C3A-n2	6.1 (2)	<i>T. convexa</i>
B <i>Thalassiosira praeconvexa</i>	C3A-n2	6.3 (2)	A/B boundary
T <i>Nitzschia porteri</i>	C4-n1	6.7 (2)	
B <i>Nitzschia miocenica</i>	C4-n1	6.75 (1)	<i>N. miocenica</i>
T <i>Rossiella paleacea</i>	C4-n1	6.8 (2)	
T <i>Thalassiosira burckliana</i>	C4-n2	7.0 (2)	A/B boundary
B <i>Nitzschia reinholdii</i>		7.3	
T <i>Actinocyclus ellipticus</i> var. <i>javanicus</i>	C4-n2	7.35 (1)	
B <i>Nitzschia marina</i>		7.4	
T <i>Thalassiosira yabei</i>	C4-n3	7.55 (2)	<i>N. porteri</i>
B <i>Nitzschia cylindrica</i>	C4-n3	7.55 (1)	
B <i>Azpeitia nodulifer</i> var. <i>cyclopus</i>	C4-n3	7.7 (1)	
T <i>Coscinodiscus loeblichii</i>		7.9	
B <i>Nitzschia fossilis</i>		8.1	
B <i>Thalassiosira burckliana</i>	C4A-n1	8.2 (2)	A/B boundary
B <i>Coscinodiscus loeblichii</i>		8.4	
T <i>Azpeitia vetustissimus</i> var. <i>javanica</i>	C4A-n2	8.55 (2)	
B <i>Azpeitia vetustissimus</i> var. <i>javanica</i>	C4A-n3	8.75 (2)	
T <i>Crucidenticula hustedtii</i> s.l.	C4A-n3	8.8 (1)	
T <i>Actinocyclus moronensis</i>	C4A-n3	8.9 (2)	<i>T. yabei</i>
B <i>Actinocyclus ellipticus</i> f. <i>lanceolata</i>		9.9	
T <i>Synedra jouseana</i>		10.4	
T <i>Crucidenticula punctata</i>		10.6	
B <i>Rossiella paleacea</i> var. <i>elongata</i>		10.6	
B <i>Thalassionema robusta</i>		10.6	
T <i>Coscinodiscus gigas</i> var. <i>diorama</i>		10.7	
T <i>Crasepedodiscus coscinodiscus</i>		10.7	<i>A. moronensis</i>
T <i>Actinocyclus ellipticus</i> var. <i>spiralis</i>		10.8	
B <i>Hemidiscus cuneiformis</i>	C5-n3	11.1 (2)	
B <i>Rossiella praepaleacea</i>		11.45	
T <i>Actinocyclus ingens</i>		11.5	
T <i>Cestodiscus pulchellus</i>		11.6	
B <i>Nitzschia porteri</i>		11.7	
B <i>Coscinodiscus temperi</i> var. <i>delicata</i>		11.8 (4)	<i>C. coscinodiscus</i>
T <i>Crucidenticula nicobarica</i>		12.2	
T2 <i>Annellus californicus</i>		12.4	
B <i>Coscinodiscus gigas</i> var. <i>diorama</i>		12.6	
T <i>Coscinodiscus lewisianus</i>	C5A-n4	12.8 (1)	<i>C. gigas</i> var. <i>diorama</i>
B <i>Crucidenticula punctata</i>		13.0	
T <i>Thalassiosira tappanae</i>	C5AB-n	13.2 (1)	
B <i>Azpeitia nodulifer</i>	C5AB-n	13.3 (1)	
B <i>Triceratium cinnamomeum</i>		13.4	
B <i>Denticulopsis hustedtii</i>	C5AC-n	13.65 (1)	
B <i>Actinocyclus ellipticus</i> var. <i>spiralis</i>		14.2	
T <i>Cestodiscus peplum</i>	C5AD-n	14.2 (2)	<i>C. lewisianus</i>
B <i>Actinocyclus ellipticus</i>		14.4	
B <i>Coscinodiscus blysmos</i>		14.6	
B <i>Thalassiosira tappanae</i>	C5AD-n	14.6 (1)	
T1 <i>Annellus californicus</i>		15.0	A/B boundary
T <i>Azpeitia praenodulifer</i>		15.4	
B <i>Actinocyclus ingens</i>		15.5	
T <i>Nitzschia maleinterpretaria</i>		15.6	
T <i>Coscinodiscus lewisianus</i> var. <i>similis</i>		15.7	
T <i>Crucidenticula kanayae</i>		16.0	
T <i>Thalassiosira fraga</i>		16.2	
B <i>Cestodiscus peplum</i>	C5C-n1	16.4 (1)	<i>C. peplum</i>
T <i>Synedra miocenica</i>	C5C-n1	16.5 (5)	
T <i>Raphidodiscus marylandicus</i>	C5C-n2	16.75 (5)	
B <i>Crucidenticula kanayae</i>	C5C-n3	16.9 (5)	
T <i>Thalassiosira bukryi</i>	C5C-n3	17.0	A/B boundary
B <i>Coscinodiscus blysmos</i>	C5C-n3	17.1 (5)	
B <i>Annellus californicus</i>	C5C-n3	17.3 (5)	
B <i>Crasepedodiscus coscinodiscus</i>	C5C-n3	17.3 (5)	
T <i>Coscinodiscus lewisianus</i> var. <i>robustus</i>	C5C-n3	17.4 (5)	
B <i>Coscinodiscus lewisianus</i> var. <i>similis</i>	C5C-n3	17.4 (5)	
T <i>Thalassiosira spumellaroides</i>	C5C-n3	17.5 (5)	
T <i>Triceratium pileus</i>	C5D-n1	17.6 (5)	
B <i>Crucidenticula nicobarica</i>	C5D-n1	17.8 (1)	<i>C. nicobarica</i>
T <i>Thalassiosira spinosa</i>	C5D-n1	18.0 (5)	
T <i>Actinocyclus radionovae</i>	C5CD-n1	18.0 (5)	
T <i>Crasepedodiscus elegans</i>		18.7	<i>T. pileus</i>
B <i>Nitzschia maleinterpretaria</i>		18.8	
B <i>Triceratium pileus</i>		18.8	
T <i>Coscinodiscus rhombicus</i>	C5E-n	19.0 (1)	
T <i>Actinocyclus hajosiae</i>		19.6	
T <i>Bogorovia veniamini</i>	C6-n	19.9 (4)	<i>C. elegans</i>

Table 5 (continued).

Event	Calibration	Age (Ma)	Zone (base)
B <i>Thalassiosira fraga</i>		19.9	
B <i>Coscinodiscus lewistianus</i> var. <i>robustus</i>		20.0	
T <i>Azpeitia oligocenica</i>		20.6	B/C/boundary
T <i>Melosira architecturalis</i>		20.7	
B <i>Actinocyclus radionovae</i>	C6A	21.2 (4)	
B <i>Actinocyclus hajosiae</i>		22.0	
T <i>Thalassiosira primababiata</i>		21.7	A/B boundary
B <i>Craspedodiscus elegans</i>		22.2	
B <i>Thalassiosira spumellaroides</i>		22.2	
T <i>Coscinodiscus lewistianus</i> var. <i>rhomboides</i>		22.5	
T <i>Rocella gelida</i>		22.7	
B <i>Rossiella paleacea</i>		22.7	<i>R. paleacea</i>
B <i>Rocella gelida</i> var. <i>schraderi</i>		23.6	
B <i>Thalassiosira spinosa</i>		23.6	
B <i>Rocella gelida</i>		24.5	<i>R. gelida</i>

T=top; B=bottom; Number in parentheses indicate reference for calibration of the event to the magnetostratigraphy; 1=Barron (in press), 2=Burckle (1978); 3=Burckle and Trainer (1979); and 4=Barron et al. (1985).

1250× magnification, were identified and counted, and the abundances were estimated following the code described below.

2. To check the presence or the absence of index species in critical intervals, observations were conducted until a reasonable number of nannofossils had been scanned. This number varied depending on the abundance of marker species and on the overall abundance of nannofossils. In the case of abundant species, at least 500 specimens were observed; in the case of subordinate and rare species, the presence or absence of an index species was evaluated by observing a fixed number of specimens belonging to the same group (100–200 discoasterids, 100 helicoliths and sphenoliths, 30–50 ceratolithids).

The abundance code used is as follows (1250× magnification):

A (abundant) = usually more than 10 specimens occurring per field;

C (common) = 1–10 specimens per field;

F (few) = 1 specimen per 1–10 fields; and

R (rare) = 1 specimen per more than 10 fields.

The qualitative evaluation of the state of preservation of the calcareous nannofossils was made with the following criteria:

G (good) = specimens exhibit little or no dissolution and/or overgrowth;

M–G (moderate to good) = specimens exhibit slight to moderate dissolution and/or overgrowth, and the identification of some species is impaired;

M (moderate) = specimens exhibit moderate dissolution and/or overgrowth, and identification is impaired at specific level; and

P (poor) = specimens exhibit extreme dissolution and/or overgrowth.

These categories were determined on the basis of the “average” state of preservation of the calcareous nannofossil examined in the smear slides. Considerable variation in the preservation state of the individual specimens might be observed in any sample. We estimated the degree of etching (E) and overgrowth (O), following the criteria proposed by Roth and Thierstein (1972) and modified by Roth (1983). We recognized the following states of dissolution and overgrowth:

E-0 and O-0: no sign of dissolution and overgrowth;

E-1 and O-1: slight dissolution and overgrowth;

E-2 and O-2: moderate dissolution and overgrowth; and

E-3 and O-3: severe effects of dissolution and overgrowth.

Combinations of the different categories can occur. E-0 O-0 and E-3 O-3 represent the best preservation and the poorest preservation state, respectively.

Planktonic Foraminifers

Blow's (1969) zonal scheme, which is widely employed for tropical areas, is used here. We incorporated into this zonation the modifications proposed by Kennett and Srinivasan (1983). Correlations of planktonic foraminiferal datums with the GPTS have been summarized by Berggren et al. (1985) for the entire Neogene and by Barron et al. (1985) for the Miocene. Ages given by these authors were applied to Neogene foraminifer datums (Table 6).

Methods

Samples were disaggregated by washing them over a 63- μ m mesh sieve and then dried. Species abundances were estimated (no actual counts were done) using the following categories:

R (rare) = <3%;

F (few) = 3%–15%;

C (common) = 15%–30%; and

A (abundant) = >30%.

Preservation characteristics were divided into three categories:

G (good) = more than 90% of the specimens unbroken;

M (moderate) = 30%–90% of the specimens showing dissolved or broken chambers; and

P (poor) = samples dominated by fragments and specimens with broken or dissolved chambers.

Radiolarians

A recent study by Johnson et al. (1989) developed a detailed Pliocene–Pleistocene zonation for the tropical Indo-Pacific Ocean. This zonal scheme is built on the low-latitude zonations of Nigrini (1971) for the Quaternary and of Sanfilippo et al. (1985) for the Tertiary. The key species used in this zonation also are found in the tropical Pacific and were used in the study of the Leg 138 samples (Table 7). Combining Johnson et al.'s zonation with that of Sanfilippo et al. does present a problem, however. Both zonal schemes contain a *Stichocorys peregrina* Zone—each with a different definition. The *Stichocorys peregrina* Zone of Johnson et al. (from the last

Table 6. Estimated ages of planktonic foraminiferal species events used during Leg 138 based on the paleomagnetic time scale of Berggren et al. (1985).

Event	Age (Ma)	Zone (base)
T <i>Globigerinoides fistulosus</i>	1.6	
B <i>Globigerina calida calida</i>		N23
T <i>Globigerinoides obliquus extremus</i>	1.8 (1.16–1.90)	
B <i>Globorotalia truncatulinoides</i>	1.9 (1.5–1.9)	N22
T <i>Globoquadrina altispira</i>	2.9 (2.8–2.99)	
B <i>Globigerinoides fistulosus</i>	2.9	
T <i>Sphaeroidinellopsis</i> spp.	3.0 (2.90–3.04)	
B <i>Globorotalia tosaensis</i>	3.1	N21
T <i>Pulleniatina primalis</i>	3.5	
T <i>Pulleniatina spectabilis</i>	3.9	
T " <i>Globigerina</i> " <i>nepenthes</i>	3.9 (3.96–4.7)	
B <i>Globorotalia crassaformis</i>	4.3	
B <i>Sphaeroidinella dehiscens</i>	5.1	N19
B <i>Globorotalia tumida</i>	5.2	N18
B <i>Pulleniatina spectabilis</i>	5.2	
B <i>Globigerinoides conglobatus</i>	5.3	
T <i>Globoquadrina dehiscens</i>	5.3	
B <i>Pulleniatina primalis</i>	5.8	N17b
B <i>Neogloboquadrina humerosa</i>	7.5	
B <i>Globorotalia plesiotumida</i>	8.0 (8.8–9.3)	N17a
B <i>Neogloboquadrina acoastaensis</i>	10.2 (10.1–10.3)	N16
T <i>Globorotalia siakensis</i>	10.4	N15
B " <i>Globigerina</i> " <i>nepenthes</i>	11.3	N14
B <i>Sphaeroidinellopsis subdehiscens</i>	11.8	N13
B <i>Globorotalia fohsi lobata</i>	^a 13.5	N12
B <i>Globorotalia praefohsi</i>	14.0	N11
B <i>Globorotalia peripheroacuta</i>	^a 14.6	N10
B <i>Orbulina suturalis</i>	15.2	N9
B <i>Praeorbulina sicana</i>	^a 16.3	N8
T <i>Catapsydrax dissimilis</i>	17.6	N7
B <i>Globigerinatella insueta</i>	^a 17.9	N6
T <i>Globorotalia kugleri</i>	^a 20.1	N5
B <i>Globoquadrina dehiscens</i>	^a 21.2	N4b
B <i>Globorotalia kugleri</i>	23.7	N4a

Notes: T=top; B=bottom. Age estimates are based on Berggren et al. (1985) unless otherwise noted. Ages in parentheses are those given by Weaver and Clement (1987) obtained at DSDP sites 606 to 611. Ages from Barron et al. (1985) are indicated by "^a".

occurrence of *Phormostichoartus fistula* to the last occurrence of *Stichocorys peregrina* was used here. The range of *Anthocorytis prolatum* defines the lowermost zone in the scheme set up by Johnson et al. and encompasses much of the lower part of the *Stichocorys peregrina* Zone, as defined by Sanfilippo et al. Unfortunately, this species was not found in the central equatorial Pacific (Nigrini and Caulet, 1988), nor was it found consistently in the material studied from Leg 138. Thus, the zonation of Johnson et al. was changed and a new zone has been introduced between the base of the *Phormostichoartus doliolum* Zone and the top of the *Didymocyrtis penultima* Zone. The top of this interval is defined by the last appearance of *Solenosphaera omnitubus*, and its base is defined by the evolutionary transition from *Stichocorys delmontensis* to *Stichocorys peregrina*. This latter evolutionary event is the same as that used by Sanfilippo et al. to define the top of the *Didymocyrtis penultima* Zone; thus, this change closely links and unifies the zonation of Sanfilippo et al. with that of Johnson et al. This new zone is called the *Solenosphaera omnitubus* Zone. It contains the last occurrence of *Acrobotryis tritubus* in most tropical regions of the Indian and Pacific oceans (Johnson and Nigrini, 1985) and apparently spans the Pliocene/Miocene boundary.

Methods

Sample preparation for the radiolarian study followed the procedures described in Sanfilippo et al. (1985). All samples were treated with acid and sieved at 63 μ m, with the coarse fraction retained for

Table 7. Estimated ages of Neogene radiolarian events used during Leg 138 based on the paleomagnetic time scale of Berggren et al. (1985).

Datum	Age (Ma)	Zone (base)
B <i>Buccinosphaera invaginata</i>	* 0.12–0.18 (1)	<i>B. invaginata</i>
T <i>Stylatractus universus</i>	0.41 (2)	<i>S. universus</i>
B <i>Collosphaera tuberosa</i>	* 0.6–0.7 (1)	<i>C. tuberosa</i>
T <i>Lamprocyrtis neoheteroporos</i>	0.946–0.965 (3)	
T <i>Anthocorytidium angulare</i>	1.047–1.052 (3)	<i>A. ypsilon</i>
T <i>Theocorythium vetulum</i>	1.088–1.11 (3)	
B <i>Lamprocyrtis nigrinia</i>	**1.27–1.29 (3)	
B <i>Theocorythium trachelium</i>	1.36–1.37 (3)	
B <i>Pterocorys minithorax</i>	1.455–1.48 (3)	
B <i>Anthocorytidium angulare</i>	1.54–1.56 (3)	
T <i>Pterocanium prismatium</i>	1.60–1.62 (1)	<i>A. angulare</i>
B <i>Theocalyptra davisiana</i>	2.565–2.60 (3)	
T <i>Anthocorytidium jenghisi</i>	2.1–2.5 (1)	<i>P. prismatium</i>
T <i>Stichocorys peregrina</i>	2.5–2.78 (1)	<i>A. jenghisi</i>
T <i>Anthocorytidium pliocenica</i>	2.71–2.73 (1,3)	
B <i>Lamprocyrtis neoheteroporos</i>	2.9–3.3 (1)	
T <i>Phormostichoartus fistula</i>	3.1–3.2 (1)	<i>S. peregrina</i>
T <i>Lychnodictyum audax</i>	**3.0–3.5 (1)	
T <i>Spongaster pentas</i>	3.4–3.5 (1)	
T <i>Phormostichoartus doliolum</i>	3.5–3.6 (1)	<i>P. fistula</i>
B <i>Amphirhopalum ypsilon</i>	3.6–3.8 (1)	
B <i>Spongaster tetras</i>	3.7–3.9 (1)	
T <i>Spongaster berminghami</i>	**4.2–4.6 (1)	
B <i>Spongaster pentas</i>	**4.3–5.1 (1)	
B <i>Anthocorytidium prolatum</i>	–	
T <i>Solenosphaera omnitubus</i>	4.7–4.8 (4)	<i>P. doliolum</i>
T <i>Stichocorys delmontensis</i>	4.9	
T <i>Siphostichartus corona</i>	4.9–5.2 (4)	
T <i>Acrobotryis tritubus</i>	5.3–5.5 (4)	
T <i>Stichocorys johnsoni</i>	5.8–6.0 (4)	
<i>Stichocorys delmontensis</i>	–	
> <i>S. peregrina</i>	**6.1–6.7 (4)	<i>S. omnitubus</i>
T <i>Calocyclus caepa</i>	**6.2–6.8 (4)	
T <i>Solenosphaera omnitubus</i>	6.4–6.8 (4)	
T <i>Diartus hughesi</i>	6.7–7.1 (4)	
B <i>Stichocorys peregrina</i>	–	
B <i>Acrobotryis tritubus</i>	**7.7–7.78 (4)	
B <i>Spongaster berminghami</i>	**7.9–8.0 (4)	
T <i>Stichocorys wolffii</i>	8.0–8.2 (4)	
T <i>Botryostrobus miralestensis</i>	**8.1–8.2	
T <i>Didymocyrtis laticonus</i>	–	
T <i>Diartus pettersoni</i>	**8.1–8.2 (4)	
<i>Diartus pettersoni</i>	–	
> <i>Diartus hughesi</i>	8.3–8.6 (4)	<i>D. antepenultima</i>
T <i>Stichocorys wolffii</i>	8.1–8.2 (4)	
B <i>Botryostrobus bramlettei</i>	8.8–8.9 (4)	
B <i>Diartus hughesi</i>	**8.7–8.8 (4)	
T <i>Lithopera thornburgi</i>	–	
T <i>Cyrtocapsella cornuta</i>	11.6–11.9 (4)	
B <i>Diartus pettersoni</i>	**12.5–12.7 (4)	<i>D. pettersoni</i>
T <i>Dorcadospyrus alata</i>	*13.5–13.7 (4)	
B <i>Calocyclus caepa</i>	–	
T <i>Calocyclus virginis</i>	–	
<i>Didymocyrtis violina</i>	–	
> <i>Didymocyrtis laticonus</i>	–	
T <i>Calocyclus costata</i>	15.0 (4)	
<i>Dorcadospyrus dentata</i>	–	
> <i>Dorcadospyrus alata</i>	16.7	<i>D. alata</i>
T <i>Stichocorys diaphenes</i>	–	
B <i>Calocyclus costata</i>	17.3	<i>C. costata</i>
T <i>Lycnecanium elongata</i>	–	
<i>Didymocyrtis mammiferus</i>	–	
> <i>Didymocyrtis violina</i>	–	
B <i>Dorcadospyrus dentata</i>	–	
B <i>Siphostichartus corona</i>	–	
B <i>Stichocorys wolffii</i>	19.2	<i>S. wolffii</i>
T <i>Dorcadospyrus atuechus</i>	–	
B <i>Stichocorys delmontensis</i>	–	
T <i>Theocyrtis annosad</i>	21.0	<i>S. delmontensis</i>
<i>Calocyclus robusta</i>	–	
> <i>Calocyclus virginis</i>	–	
T <i>Calocyclus serrata</i>	–	
B <i>Cyrtocapsella tetrapera</i>	22.6	<i>C. tetrapera</i>
B <i>Cyrtocapsella cornuta</i>	–	

Notes: T=upper morphotypic, B=lower morphotypic, and >=evolutionary transition. Number in parentheses indicate the references for age estimates of the events. Sources for age estimates are: 1=Johnson et al. (1989), 2=Hays and Shackleton (1976), 3=Alexandrovitch (1991), 4=Johnson and Nigrini, (1985). Single age estimates are approximations from interpolations and from Berggren et al. (1985). An asterisk (*) denotes that the age of the event is established only in the Indian Ocean, whereas a double asterisk (**) indicates events which are (or might be) diachronous.

slide preparation. When the acid-treated residues contained large clumps of clay aggregates, the coarse fraction was further treated with a strong base (NaOH) for several minutes, then briefly immersed in an ultrasonic bath and resieved.

The recorded abundance of radiolarians in each sample was based on qualitative examination of strewn slides of sieved acid residues. Consequently, discrepancies may exist between these observations and those in the lithologic smear slide reports. Abundances are recorded as follows:

- C (common) = 100–500 specimens in the noncalcareous fraction;
- F (few) = 10–100 specimens; and
- R (rare) = 3–10 specimens.

The preservation of radiolarians in the strewn slides is defined as follows:

- G (good) = no (to very slight) dissolution effects;
- M (moderate) = dissolution observed, but minor; and
- P (poor) = strong dissolution effect.

Diatoms

Numerous diatom biostratigraphic studies have been completed for the equatorial Pacific (Burckle, 1972, 1977, 1978; Burckle and Trainer, 1979; Barron 1980, 1981, 1983, 1985a, 1985b, in press; Baldauf, 1985; and Sancetta, 1984). The Neogene and Quaternary diatom zonation used during Leg 138 was that proposed by Barron (1985a, 1985b). This zonation consists of 18 zones and 20 subzones. The majority of markers used for this zonation have been directly calibrated to magnetostratigraphy based on the studies of Burckle (1978); Burckle et al. (1982); Barron (1985b, in press); and Barron et al. (1985). Table 5 lists diatom biostratigraphic events, paleomagnetic calibration, and age estimates used during this leg.

Methods

Smear slides were examined on a routine basis for stratigraphic markers. When required (because of low concentration of specimens), selected samples were processed using hydrogen peroxide and hydrochloric acid, following a modified version of the procedures of Baldauf (1984). Strewn slides of the acid-clean material were examined using magnifications between 750 \times and 1250 \times .

Abundance of diatoms was based on the number of specimens observed per field of view at (750 \times). These abundances were recorded as follows:

- A (abundant) = 2 or more specimens per field of view;
- C (common) = 1 specimen per field of view;
- F (few) = 1 specimen per each horizontal transverse; and
- R (rare) = <1 specimen per each horizontal transverse.

Preservation of diatoms was determined qualitatively and was recorded as follows:

- G (good) = both finely silicified and heavily robust forms were present, and no alteration of the frustules was observed;
- M (moderate) = finely silicified forms were present, but exhibit some alteration; and
- P (poor) = finely silicified forms were rare or absent, and the assemblage was dominated by robust forms.

Sedimentation Rates and Accumulation Rates

Methods

The primary data for estimating sedimentation rates are the depth below seafloor at which each datum is located and the age assigned to that datum. In a site having precisely determined paleomagnetic stratigraphy and with unambiguously identified chrons, uncertainties about accumulation rates arise almost entirely from the uncertainties in the reversal time scale. Here, we use that given by Berggren et al. (1985) (Table 3). For the Pleistocene–Pliocene, alternative versions have been proposed that are based on tuning to the periods of Earth's orbital geometry (for example, Shackleton et al., 1990). However, although these versions in principle are more accurate, we do not use them because it is unclear how these should be integrated with the available time scale for the older section. This would depend whether the offset is systematic and dependent on the half-lives involved, or arises from particular difficulties in dating young volcanic rocks. Scientists usually assume that even if the time scale has uncertainties, these will not give rise to rapid changes in apparent accumulation rate because average seafloor spreading rates, on which the time scale depends, are unlikely to change suddenly. This assumption is becoming testable with the advent of orbital tuning methods, and one objective of Leg 138 is to obtain high-resolution records (GRAPE, magnetic susceptibility, and color reflectance aboard ship and several other types of data post-cruise) that will bring us closer to that goal.

Where biostratigraphic datums are used, the chief uncertainty arises from the fact that with a limited amount of time available, many datums are determined between widely separated limits; during many ODP legs, it has been necessary to reconstruct sedimentation rates from datums defined only between core catchers (i.e., within 9.5 m). The uncertainty in each accumulation rate estimate arising from this source is the thickness interval over which it is averaged, divided by the combined uncertainty in the top and bottom controls. At a sedimentation rate of 20 m/m.y., datums spaced at 9.5-m intervals would only justify breaking the accumulation rates in roughly 4-m.y. increments if we aim for an uncertainty better than $\pm 20\%$.

The second uncertainty, of course, is the age of the datums; this uncertainty would be equally large in the above example, were the datum ages determined within limits of about 0.5 Ma. Our aim is to use a prime set of datums, distributed less than 2 m.y. apart, and to determine these datums in all sites to within one section (1.5 m) or better. Only the calcareous nannofossils can provide datums at a 2-m.y. spacing for the entire time interval to be covered in Leg 138 whose ages have been determined with appropriate precision, and even here there are parts of the Miocene where the true uncertainty is far worse because of potential errors in correctly identifying equivalents of identified seafloor anomalies, in particular, fossiliferous sequences.

Tables 4 and 5 give the biostratigraphic datums that have been positioned relative to the magnetic anomaly time scale with varying degrees of precision and confidence. Sedimentation rates may be estimated from age-vs.-depth plots either by drawing best-fit lines through all the data, or by drawing straight-line segments (uniform sedimentation rate) between selected datums. For best comparison between sites, and to make optimum use of the most precisely determined datums, we have chosen the second solution. Inspection of the distribution of other datums about the lines suggests that it might be difficult to rigorously justify one approach vs. another, especially given the difficulty when evaluating the uncertainties in the accuracy of each datum. Note that, although plots of sedimentation rate vs. age give the most accurate portrayal of the actual rates and fluxes, the distribution of data points in the age-vs.-depth plots may give a better impression of the evidence for or against rapid changes

Table 8. Depths of tops and bottoms of each core from Site 844.

Core	Depth (mbsf)	Core (m)	Depth (mcd)	Offset (m)
138A-				
844A-1H	0-9.94	9.94	1.40-11.34	1.40
844B-1H	0-4.53	4.53	0-4.53	0.00
844B-2H	4.50-14.48	9.98	5.63-15.61	1.13
844B-3H	14.00-24.05	10.05	16.25-26.30	2.25
844B-4H	23.50-33.48	9.98	14.95-24.93	8.55
844B-5H	33.00-42.90	9.90	36.65-46.55	3.65
844B-6H	42.50-52.52	10.02	46.60-56.62	4.10
844B-7H	52.00-62.06	10.06	58.70-68.76	6.70
844B-8H	61.50-71.46	9.96	68.65-78.61	7.15
844B-9H	71.00-81.10	10.10	79.65-89.75	8.65
844B-10H	80.50-90.27	9.77	91.13-100.90	10.63
844B-11H	90.00-99.99	9.99	103.50-113.49	13.50
844B-12H	99.50-109.59	10.09	113.03-123.12	13.53
844B-13H	109.00-118.95	9.95	122.80-132.75	13.80
844B-14H	118.50-128.26	9.76	133.33-143.09	14.83
844B-15H	128.00-137.82	9.82	143.00-152.82	15.00
844B-16H	137.50-147.43	9.93	153.68-163.61	16.18
844B-17H	147.00-157.07	10.07	162.60-172.67	15.60
844B-18H	156.50-166.43	9.93	173.55-183.48	17.05
844B-19H	166.00-175.83	9.83	183.20-193.03	17.20
844B-20H	175.50-185.58	10.08	194.13-204.21	18.63
844B-21X	185.00-194.69	9.69	203.63-213.32	18.63
844B-22X	194.60-204.27	9.67	213.23-222.90	18.63
844B-23X	204.30-213.90	9.60	222.93-232.53	18.63
844B-24X	213.90-223.65	9.75	232.53-242.28	18.63
844B-25X	223.60-232.04	8.44	242.23-250.67	18.63
844B-26X	233.30-243.06	9.76	251.93-261.69	18.63
844B-27X	242.90-243.30	0.40	261.53-261.93	18.63
844B-28X	252.60-261.66	9.06	271.23-280.29	18.63
844B-29X	261.90-271.75	9.85	280.53-290.38	18.63
844B-30X	271.60-281.47	9.87	290.23-300.10	18.63
844B-31X	281.20-291.25	10.05	299.83-309.88	18.63
844C-1H	0-9.10	9.10	0.50-9.60	0.50
844C-2H	9.10-18.62	9.52	10.40-19.92	1.30
844C-3H	18.60-28.66	10.06	20.95-31.01	2.35
844C-4H	28.10-38.18	10.08	32.25-42.33	4.15
844C-5H	37.60-47.56	9.96	42.85-52.81	5.25
844C-6H	47.10-57.20	10.10	53.75-63.85	6.65
844C-7H	56.60-66.73	10.13	64.25-74.38	7.65
844C-8H	66.10-76.30	10.20	75.41-85.61	9.31
844C-9H	75.60-85.78	10.18	85.78-95.96	10.18
844C-10H	85.10-94.92	9.82	96.11-105.93	11.01
844C-11H	94.60-104.66	10.06	106.55-116.61	11.95
844C0-12H	104.10-114.15	10.05	116.10-126.15	12.00
844C-13H	113.60-123.62	10.02	126.60-136.62	13.00
844C-14H	123.10-132.71	9.61	138.10-147.71	15.00
844C-15H	132.60-142.80	10.20	147.50-157.70	14.90
844C-16H	142.10-152.16	10.06	157.60-167.66	15.50
844C-17H	151.60-161.50	9.90	168.60-178.50	17.00
844C-18H	161.10-171.19	10.09	178.05-188.14	16.95
844C-19H	170.60-180.80	10.20	189.95-200.15	19.35
844D-1H	24.00-34.12	10.12	28.70-38.82	4.70

Notes: Table gives tops and bottom in original meters below seafloor (mbsf) as determined by drill pipe length. Top and bottom is given in meters composite depth (mcd) as well as offset constant needed to convert mbsf to mcd (=mbsf+offset).

in sedimentation rate, because the method we used tends to exaggerate the suddenness of the changes.

As regards the use of linear sedimentation rates to determine burial fluxes, note that "ODP depths" measured by the drill string are probably more accurate in regard to long-term fluxes in that this is a better means of measuring actual thickness than the on-deck measurement of a composite section that may be physically stretched.

Sediment accumulation rates are calculated from linear sedimentation rates using so-called dry bulk density (g dry sediment per wet ml). Given the difficulty in attaining better than $\pm 20\%$ accuracy in linear sedimentation rate, uncertainties in density are a minor factor (although strictly speaking, we should use an *in-situ* density because the drill string measures *in-situ* thickness). We have used mean values for the appropriate intervals. Accumulation rates of calcium carbonate are first expressed in the same way (i.e., using mean values). Higher-frequency variations in percentage of carbonate obviously imply that superimposed on relatively stable long-term accumulation rates are higher-frequency variations in accumulations of either carbonates or noncarbonates.

COMPOSITE DEPTHS

Composite Section Development

The recovery of complete, uninterrupted sedimentary sections was of primary importance to the objectives of Leg 138. To document the continuity of the recovered section as well as to guide drilling operations,

composite depth sections were developed at all multiple-cored sites using shipboard measurements of magnetic susceptibility, GRAPE, and percent reflectance. This section briefly explains the methods used for developing composite sections for each site. A more detailed discussion of the construction of composite sections and adjustments to the depth scale may be found in Hagelberg et al. (this volume).

At each site, high-resolution (5-cm intervals or less) measurements of GRAPE, magnetic susceptibility, and percentage of reflectance were performed soon after the cores were retrieved. These measurements then were entered into the shipboard data base. During drilling of additional holes at each site, these three signals were compared to ensure that coring offsets were maintained between holes. Upon completion of drilling at the site, each of these three signals at adjacent holes were compared. The visual comparison of these signals allowed us to correlate hole-to-hole. For a given type of measurement, these correlations were performed by adjusting the ODP sub-bottom depths for a given core, on a core-by-core basis. No depths were adjusted within a given core. The results from each of the three measurements (GRAPE, magnetic susceptibility, and percentage of reflectance) then were integrated to resolve discrepancies, which resulted in a single composite depth section for the site. The results of this integration for a site are given in each of the site chapters.

The composite depth section for each site is presented in a tabular format; an example is given in Table 8. For each hole drilled, the ODP sub-bottom depth (in meters below seafloor, or mbsf) for the top and bottom of each core is listed in Column 2. Column 3 lists the length (in meters) of the individual core. In Column 4, the composite depth (in meters composite depth, or mcd) for the top and bottom of each core is listed. Column 5 gives the amount of constant offset applied to the ODP sub-bottom depth for that core. This column facilitates conversion of samples that are recorded in ODP sub-bottom depths to composite section depth. By adding the amount of offset listed in Column 5 to the ODP sub-bottom depth of a measurement taken in a particular core, the equivalent composite sub-bottom depth is obtained. Thus, this table can be used as a sampling strategy guide.

PALEOMAGNETISM

Laboratory Facilities

The paleomagnetic laboratory on board the *JOIDES Resolution* is equipped with two magnetometers: a pass-through cryogenic superconducting rock magnetometer manufactured by 2-G Enterprises (Model 760R) and a Molspin spinner magnetometer. To remove secondary magnetizations in discrete samples, we used a Schonsted model GSD-1 alternating field (AF) demagnetizer capable of demagnetizing discrete specimens to 100 mT. In addition, in line with the pass-through cryogenic magnetometer is an AF demagnetizer capable of 25 mT (2-G Model 2G600).

The sensing coils in the cryogenic magnetometer measure signal over about a 20-cm interval, and the coils for each axis have slightly different response curves. The widths of the sensing regions correspond to about a 200- to 300-cm³ volume of cored material that contributes to the signal at the sensors. The large volume of core material within the sensing region permits accurate determination of the remanence for weakly magnetized samples, despite the relatively high background noise related to the motion of the ship. In fact, the practical limit on the sensitivity seems to be imposed by the magnetization of the core liner itself (which is equivalent to a standard volume of sediment with magnetization of about 0.1 mA/m = 10^{-7} emu/cm³).

The pass-through cryogenic magnetometer and its AF demagnetizer interface with an IBM PC-AT-compatible computer and are controlled by a BASIC program modified from the original SUPERMAG program. We noted that the current version of the SUPERMAG program was previously modified to compensate for end effects. To do so, the program divides the sensor output by the portion of the area under the response curves contained in sediment. The spinner magnetometer used for measuring discrete samples interfaced with a Macintosh SE/30 using a program brought on board during Leg 138.

The magnetic susceptibility of unsplit sections of core was measured with Bartington Instruments's Model MS1 susceptibility meter adapted with a MS1/CX 80-mm whole-core sensor loop set at 4.65 kHz. The full width of the impulse response peak at half maximum is less than 5 cm. The susceptibility sensor is mounted with the GRAPE and *P*-wave logger on the MST. Susceptibility of discrete specimens can be measured on board the ship with a sensor unit (type MS1B) that attaches to the Bartington susceptibility meter.

Paleomagnetic Measurements

Pass-Through Magnetometer

Most of the paleomagnetic measurements performed during Leg 138 were done using the pass-through cryogenic magnetometer. While steaming from port to the first site, we conducted several tests with discrete calibration samples, which had been brought on board ship (1) to ascertain if the instrument was behaving satisfactorily, (2) to establish the accuracy of our basic measurements, and (3) to check our processing software.

Pass-through paleomagnetic measurements were routinely performed on the archive halves of the 1.5-m core sections. The ODP core orientation scheme arbitrarily designates the *X*-axis as the horizontal (*in-situ*) axis radiating from the center of the core through the space between a double line scribed lengthwise on the working-half of each core liner. Relative declinations were measured with respect to this double line. The natural remanent magnetization (NRM) and remanence measurements after the 10 or 15 mT AF demagnetization were routinely measured at 5-cm intervals. (Occasionally, the measuring interval of the NRM and, more rarely, the demagnetized remanence were increased to 10 cm. This was done either when the magnetic signal was very weak and it was apparent that the magnetic polarity could not be resolved, or to accelerate core-flow through the laboratory.)

The NRM generally was dominated by a vertical magnetization upward, presumably acquired during coring. Still, the NRM measurements contain important information about the expected magnetization of the sediment and possibly the origin of the overprinting. The magnetostratigraphic interpretations for Leg 138 are based on the pass-through measurements of the demagnetized cores, checked by results from discrete specimens measured with the spinner magnetometer. Data from core segments that are clearly physically disturbed, sometimes up to 50 cm from core tops, have been deleted from the data files. Other segments of core, which are magnetically noisy and uninterpretable or have an insufficient magnetic signal, were excluded from the shipboard analysis, but the data are retained in the primary ODP data files, according to the conventions described below.

Data Archiving

We adopted the following conventions for archiving data generated with the pass-through magnetometer. Following usual procedures, data files for each section were processed to create files containing data at one demagnetization level for an entire core. These files (given a .WCC extension) have not been edited or manipulated, except to correct gross errors (e.g., when the wrong section name was given or when a working-half or improperly split section required reorientation). Editing of physically disturbed intervals and voids within sections was performed with a second set of files created to reorient entire cores. These reoriented and edited files were given one of three suffixes: MOR, SOR, or UOR. Files named .MOR have been oriented with the multishot tool (see discussion below); files named .SOR have been oriented by inference based on the paleomagnetic results themselves; files named .UOR are unoriented, but have had physically disturbed intervals removed. We also concatenated individual oriented core files into files that contain results for an entire hole. These files were given a name that reflects which cores they include. Data in these hole files have been edited more freely to remove data that we presumed did not reflect the true magnetization direction in the

sediment. This level of editing typically eliminated data from within 10 cm of section breaks and 40 cm of core tops.

Core Orientation

Because of the equatorial latitudes of the Leg 138 sites, azimuthal orientation of the piston cores is important for interpreting magnetostratigraphy of the cored sequences. Core orientation of the APC cores was achieved with an Eastman-Whipstock multishot tool, which was rigidly mounted onto the coring barrel and consists of a magnetic compass and a camera. The battery-operated camera photographs continuously at prescribed intervals from 0.5 to 2 min from the time it leaves the deck. At the bottom of the hole, the core barrel is allowed to rest for sufficient time (2–8 min) to settle the compass needle and to make sure that several photographs are taken before the corer is shot into the sediment. (The photographs used for orientation are those taken just prior to shooting the core barrel into the sediment.) Orientation is not usually attempted for the top three cores (about 30 m), until the bottom-hole assembly is sufficiently stabilized in the sediment. Core orientation by the multishot camera generally was successful during Leg 138, with a subjective accuracy estimate of 20°–30°, and it contributed to our magnetostratigraphic interpretations. Exceptions to this typical performance have been noted in the site chapters. Complete multishot results obtained during the cruise have been written to the VAX file, "MULTISHOT.RESULTS."

Magnetostratigraphy

To maximize our chances for successfully determining the magnetostratigraphy and to satisfy sampling needs of the shipboard paleomagnetists (who are interested in high-resolution studies of reversals and excursions), an effort was made to take most of the shipboard samples, including whole-round geochemical and physical properties samples from the "A" holes at each site, leaving the initial post-cruise sampling of the "B" holes for such paleomagnetic studies. The "A" and "B" holes, respectively, refer here to the first and second complete APC sections at each site (e.g., Holes 844B and 844C, respectively, at Site 844).

Whenever possible, we offer in the site chapters an interpretation of the magnetic polarity stratigraphy using the magnetic polarity time scale modified from Berggren et al. (1985) (Table 3; Fig. 8). We have added three short geomagnetic features observed with sufficient regularity that they may be useful stratigraphic markers for regional/global correlations: the Blake feature at about 0.1 Ma in the Brunhes and the Cobb Mountain at 1.1 Ma and the Reunion event(s) between 2.1 and 2.2 Ma in the Matuyama (Mankinen and Dalrymple, 1979). For the upper part of the time scale (roughly Pliocene–Pleistocene), we use the traditional proper or place names to refer to various chrons and subchrons. For older intervals, we follow the convention of using correlative anomaly numbers prefaced by the letter "C." Normal polarity subchrons are referred to by adding suffixes (-n1, -n2), which increase with age. The reversal boundaries themselves are specified by the chron/subchron designation, followed by the letter "o" (for onset) or "t" (for termination). Reverse polarity chrons or subchrons are similarly named with an "R" suffix (the reverse polarity portion of a chron being older than the corresponding normal polarity).

Low-Field Susceptibility

Whole-core susceptibilities are relatively rapid to measure, non-destructive, and provide an indication of the amount of magnetizable material in the sediment, including ferrimagnetic and paramagnetic constituents. Whole-core volume magnetic susceptibilities were measured using the automated MST. Measurements were performed at the high-sensitivity range (0.1) and in the SI mode, usually every 5 cm, depending on the available time for on-board measurements. When susceptibility decreased to a level indistinguishable from instrumental noise, we increased the measurement interval to 15 or 20 cm

to decrease measurement time and to monitor the data for potential downhole increases. Susceptibility data were archived in raw instrument meter readings and are presented on the barrel sheets. To convert these values to susceptibility units, one must multiply by 0.63, calculated from the manufacturer's manual, to compensate for the 0.77 ratio of core diameter to coil diameter (68:88 mm). An additional multiplicative factor of 10^{-5} is necessary to complete the conversion to volume normalized SI. These factors were checked vs. values expected for distilled water. The meter was zeroed with each section, but we did not correct for instrumental baseline-drift of each 1.5-m susceptibility profile on board the ship, although the necessary parameters were recorded and can be processed onshore. Similarly, we did not correct for the effect of the plastic core liner on board the ship; for better absolute estimates at very low values of susceptibility, it would be appropriate to correct for the diamagnetic susceptibility of the liner, which generally amounts to -0.5 to -1.0 in raw instrument units. To test the temperature effect on core susceptibility measurements between their arrival on deck (5° – 15° C) and their ambient laboratory temperature (22° – 27° C), we measured the susceptibility of several sections with the MST immediately on arrival in the core laboratory. These sections were remeasured after equilibrating at room temperature, and no significant differences in these susceptibility profiles were observed. However, note that these tests were conducted on relatively highly susceptible sediments and a temperature effect may well apply to very weakly susceptible sections. During Leg 138, whole-core susceptibility measurements provided a valuable parameter for developing within-site, hole-to-hole correlations. Thus, this parameter served to maintain adequate overlap in multiply cored sites. Apparently, meaningful correlations sometimes were possible down to low meter readings near zero and, occasionally, in the negative, diamagnetic, region.

INORGANIC GEOCHEMISTRY

Sampling and Chemistry of Interstitial Waters

Shipboard analyses of interstitial water were performed on 5- to 10-cm-long whole-round sections that were cut immediately after their arrival on deck. Interstitial waters were collected by applying pressure to the sediment using a titanium squeezer. Before being squeezed, core surfaces were carefully scraped with a spatula to remove the potentially contaminated exterior of the sample. Then, the core was placed into the piston and squeezed using a hydraulic press at pressures up to 40,000 psi. The water was collected in a plastic syringe and filtered through a $0.4\ \mu\text{m}$ disposable filter.

Interstitial water samples were routinely analyzed for alkalinity, pH, and salinity, and for concentrations of chloride, sulfate, calcium, magnesium, ammonia, and silica using the analytical techniques described by Gieskes and Peretsman (1986). Concentrations of strontium, lithium, and potassium were measured by atomic absorption spectrophotometry. Sodium concentrations were calculated by charge balance. Most measurements were calibrated with International Association of Physical Sciences Organizations (IAPSO) standard seawater. Results are expressed as millimole per liter (mM) or micromole per liter (μM).

Alkalinity and pH were measured using a Metrohm autotitrator with a Brinkmann combination electrode. The pH of IAPSO water during Leg 138 was 7.88 ± 0.04 . Alkalinity was determined by Gran titration, and the reproducibility of repeated determinations of IAPSO water during the leg was 3.5% (2.525 ± 0.089 mM).

Salinity was determined using a Golberg hand-held refractometer. This measurement is unitless, and the measurement is precise to ± 0.5 .

Sulfate was measured using a Dionex 2120i chromatograph. One-half mL aliquots of pore water were diluted to 250 mL with deionized water. Reproducibility was determined to be 1.3%; duplicate measurements of a 28.90 mM standard gave an average concentration of 28.87 ± 0.36 mM.

Chloride was measured by silver nitrate titration of 0.1-mL aliquots of sample diluted with 5 mL of deionized water; potassium chromate was used as the indicator. The chloride concentration of IAPSO water was reproducible to $\pm 0.4\%$.

Calcium was determined on a 500- μL aliquot of sample diluted to approximately 5 mL with deionized water using the titration method of Tsunogai et al. (1968), which relies on the complexation of calcium with ethylene-bis-(oxyethylenetriolo)-tetra-acetic acid (EGTA) and uses 2,2'-ethane-diylidene-dinitrilo-diphenol (GHA) as the indicator. Near the end of the titration, 2 mL of butanol is added to concentrate the Ca-GHA complex and to focus the color change at the end point. Reproducibility for replicate analyses of IAPSO seawater during Leg 138 was $\pm 0.9\%$.

Magnesium was calculated after determining the total alkaline earths (Ca^{+2} , Mg^{+2} , and Sr^{+2}). Total alkalis were determined by titration with di-sodium ethylenediamine-tetra-acetate (EDTA-sodium salt) using Eriochrome-Black-T as the indicator. Reproducibility of the IAPSO seawater standard was 0.4%.

Silica was determined by production of silicomolybdate complex and its reduction to give a blue color, which was measured at 812 nm using a Milton Roy Spectronic 1001 spectrophotometer. The reported reproducibility of this method is $\pm 3\%$.

Ammonium concentrations were determined using Solorzano's method (1969), modified by Gieskes and Peretsman (1986). This method is based on the diazotization of phenol and the subsequent oxidation of the diazo complex by chlorox to yield a blue color that was then measured with a Milton Roy spectrophotometer at 640 nm. Reported reproducibility of this technique is $\pm 3\%$. Blanks are a problem with this procedure, which limited the detection limit of ammonium during Leg 138 to 10 μM .

A Varian SpectrAA-20 spectrophotometer was used to determine concentrations of strontium, lithium, and potassium. Strontium was measured by absorption using a hollow-cathode lamp, while lithium and potassium were measured in emission mode. All measurements were performed using an oxidizing air-acetylene flame.

Concentrations of strontium were measured in 1:6 dilutions using a lanthanum trichloride solution (5000 ppm). Reproducibility of IAPSO seawater was $\pm 5\%$.

Lithium was determined in 1:6 dilutions using 0.1N HCl. Reproducibility measuring dilutions of IAPSO seawater was $\pm 3\%$.

Potassium was measured by emission AA after taking 4.5 mL of the sample diluted for the sulfate analysis and adding 0.5 mL of 1% CsCl solution to suppress ionization. Reproducibility of IAPSO seawater treated in the same way was $\pm 7\%$.

X-Ray Fluorescence Analysis

Prior to analysis, samples normally were crushed in the Spex 8510 shatterbox with a tungsten carbide barrel. This produced some tantalum and massive tungsten contamination of the sample.

A fully automated wavelength-dispersive ARL8420 XRF (3λ) system equipped with an Rh target X-ray tube was used to determine the abundances of major oxides in bulk sediment samples. Analyses of the major oxides were performed on lithium borate glass disks that had been doped with lanthanum as a "heavy absorber" (Norrish and Hutton, 1969). The disks were prepared from 500 mg of ground sediment, ignited for 2 hr at about 1030° C, and then mixed with 6.0 g of dry flux consisting of 80% lithium tetraborate and 20% La_2O_3 . This mixture then was melted at 1150° C in a Pt-Au crucible for about 10 min and poured into a Pt-Au mold using a Claisse fluxer. The 12:1 flux-to-sample ratio (and the use of the lanthanum absorber) made matrix effects insignificant over the normal range of igneous rock compositions. Hence, the following linear relationship between X-ray intensity and concentration holds true:

$$C_i = (I_i \times m_i) - b_i,$$

where

- C_i = the concentration of oxide i (wt%);
 I_i = the net peak X-ray intensity of oxide i ;
 m_i = the slope of the calibration curve for oxide i (wt%/cps); and
 b_i = apparent background concentration for oxide i (wt%).

The slope, m_i , was calculated from a calibration curve derived from the measurement of well-analyzed reference rocks (BHVO-1, G-2, AGV-1, PCC-1, JGB-1, JP-1, BR, DR-N, UBN). The background, b_i , was determined with blanks or was derived by regression analysis from the calibration curves.

Systematic errors resulting from short- or long-term fluctuations in X-ray tube intensity were corrected by normalizing the measured intensities of the samples to those of a standard that was always run together with a set of six samples. To reduce shipboard weighing errors, two glass disks were prepared for each sample. Accurate weighing was difficult on board the moving platform of the *JOIDES Resolution* and was performed with particular care; thus, because weighing errors can be a major source of imprecision in the final analysis. Loss-on-ignition (LOI) values were determined by drying the sample at 110°C for 8 hr and then weighing it before and after ignition at 1030°C.

An outline of the computation methods is presented as follows:

1. Input X-ray intensities: dead-time corrected X-ray intensities were read into the program from an ARL result file.
2. Make drift corrections: all peak and background intensities were corrected for machine drift by using a one-point correction of the form:

$$D_i = S_i/M_i, \text{ and}$$

$$I_{di} = I_i \times D_i,$$

where

- D_i = the drift factor for element i , generally 1.00 ± 0.01 ;
 S_i = the peak intensity for element i , measured on a synthetic standard ("POOP") at the time of calibration;
 M_i = the measured peak intensity for element i , measured on "POOP" at any time after the calibration;
 I_i = the uncorrected peak or background intensity, element i ;
 and
 I_{di} = the drift corrected peak or background intensity, element i .

3. Subtract backgrounds. Peak intensities were corrected for non-linear backgrounds by measuring a peak-to-average background ratio (B_{Fi}). This ratio was determined for each element using synthetic and natural blank standards at the time of calibration. Thus,

$$B_{Fi} = PK_i/AVB_{Gi}.$$

Thus, when measuring unknowns, the true or modified background (MB_{Gi}) was calculated by multiplying the average measured background for element i (AVB_{Gi}) by the B_{Fi} . This new modified background value was then subtracted from the peak intensity (PK_i) to arrive at the net peak intensity ($NETPK_i$) for element i , as

$$MB_{Gi} = AVB_{Gi} \times B_{Fi}, \text{ and}$$

$$NETPK_i = PK_i - MB_{Gi}.$$

4. Remove spectral interferences. During calibration, interferences were measured on synthetic pellets containing pure quartz and the interfering element. A ratio of the interference intensity to the net peak of the interfering element was calculated and assumed constant

with respect to concentration. When measuring an unknown, the net interference ($INTFER_{i,j}$) was calculated and removed by

$$INTFER_{i,j} = NETPK_j \times IRI_{i,j} \text{ and}$$

$$CNETPK_j = NETPK_j - INTFER_{i,j},$$

where

$INTFER_{i,j}$ = the net interference intensity of element i on element j and

$CNETPK_j$ = the net intensity of element j with the interference element i removed.

In the case of mutually interfering elements, an iterative approach to this same calculation was used until all the elements involved converge on their respective corrected values.

5. Measure mass-absorption coefficients. To correct for matrix differences among samples, three separate mass-absorption coefficients were determined following a modification of the Compton scattering technique of Reynolds (1967). Measured intensities from the rhodium K-series Compton, FeK α , and TiK α lines were compared with the calculated absorption coefficients of Rb (ARb), Cr (ACr), and V (AV), respectively. From this comparison, three equations were written to describe the relationship between each coefficient and its respective line.

By using this method, unknowns were measured and corrected for matrix differences without calculating the absorption coefficients for each sample.

6. Calculate concentrations. Once all the spectral and matrix corrections have been calculated, the equation for calculating elemental concentrations reduces to the following:

$$C_i = (CNETPK_i \times A_i)/K_i,$$

where

- C_i = the concentration of element i in parts per million;
 $CNETPK_i$ = corrected net peak intensity, element i ;
 A_i = mass-absorption coefficient for element i ; and
 K_i = calibration factor (ppm/cps) for element i .

The value K_i is analogous to the slope of the calibration curve (m_i) for major elements; it was determined in the same manner on natural rock (AGV-1, UB-N, G-2, BHVO-1, RGM-1, DRN) and synthetic (compressed, spiked quartz powders) standards.

Major-element data are precise to within 0.5% to 2.5% and are considered accurate to $\pm 1\%$ for Si, Ti, Fe, Ca, and K, and to $\pm 3\%$ to 5% for Al, Mn, Na, and P. Periodic summations to 101 to 102 wt% were observed, but were irreproducible and attributed to weighing errors or gremlins.

ORGANIC GEOCHEMISTRY

Inorganic Carbon and Percentage of Carbonate

More than 2200 sediment samples were analyzed on board the *JOIDES Resolution* for concentrations of inorganic carbon (IC). This value was used to calculate the weight percent of carbonate (%CaCO₃) in the bulk sediment. Most analyses (>95%) were on physical property samples (of approximately 10 cm³) that had previously been measured for index properties, including dry bulk density. The remaining analyses were on headspace samples (10 to 20 cm³), taken at intervals of approximately one per core for gas analysis, and on samples (5 cm³) specifically requested by the sedimentologists and chemists. The physical property samples were oven-dried, while the others were freeze-dried before grinding and homogenization. In samples from the western transect sites (Sites 848 to 854), a piece at

least 3 cm³ was removed before pulverization to preserve microfossils for future studies.

Inorganic carbon was measured with a Coulometrics 5011 CO₂ coulometer equipped with a System 140 carbonate carbon analyzer. A 10- to 60-mg sample was reacted in a solution of 2N HCl while being heated at 65° C. The evolved CO₂ was transferred to the CO₂ coulometer cell via a helium stream. The quantity of CO₂ liberated was measured by titration in a monoethanolamine solution with a proprietary colorimetric indicator. The change in light transmittance was monitored by a photodetection cell. Reagent-grade calcite was used as a standard. The %CaCO₃ was calculated from the IC concentration, assuming that all carbonate occurs as CaCO₃, as follows:

$$\%CaCO_3 = \%IC \cdot 8.334.$$

More than 300 duplicate analyses during Leg 138 indicate excellent reproducibility, with an average error of less than 0.8% CaCO₃.

Total Carbon and Total Nitrogen

We used the shipboard Carlo Erba Model 1500 CNS elemental analyzer to determine the concentrations of carbon and nitrogen in sediment samples. Results of these analyses from bulk samples or from acid-treated sample residues also were used to calculate the concentration of organic carbon in the high carbonate samples of the western transect sites (see C_{org} methods below for more details). Approximately 10 to 20 mg of bulk sample or residue was weighed into tin foil crucibles that had been cleaned with methanol and acetone prior to use. Weighing error was estimated at <0.5%, based on repeated weighing of 10- and 20-mg standard weights. In spite of the cleaning procedure, blank runs in sample crucibles (on average, one blank run per 10 samples) showed a mean of 2044 carbon counts (±1550, n = 119). Nitrogen exhibited no blank counts. To quantify the amount of carbon in a sample, we used two reliable standard substances (e.g., acetanilide and CaCO₃) to calculate response factors of the instrument to known amounts of carbon and nitrogen. The instrument response proved to be linear and reliable over the range of standards used (Fig. 10). Average values for response factors (R) were calculated using

$$R = C_{std} \cdot wt_{std} / (AC - BL),$$

where

C_{std} = concentration of element in standard,
wt_{std} = weight (in mg) of standard,
AC = area count of element, and
BL = blank count of element.

The calibration using response factors was excellent:

$$R_{carbon} = 0.000138 (\pm 0.000006, N = 103) \text{ and} \\ R_{nitrogen} = 0.000433 (\pm 0.000024, N = 52).$$

In addition to the analysis of standards and blanks (at an approximate rate of one set of blank, acetanilide, and CaCO₃ runs per 10 samples), we repeatedly measured total carbon and nitrogen in an estuarine sediment sample (NBS #1646). Based on our average calibration factors (see above), we achieved good precision for carbon (C = 1.65% ± 0.09%, n = 90) and satisfactory precision for nitrogen (N = 0.19% ± 0.05%, n = 90).

C_{org} Methods

Difference Method

The amount of C_{org} determined with the "difference method" was calculated as total carbon (measured by the elemental analyzer) minus

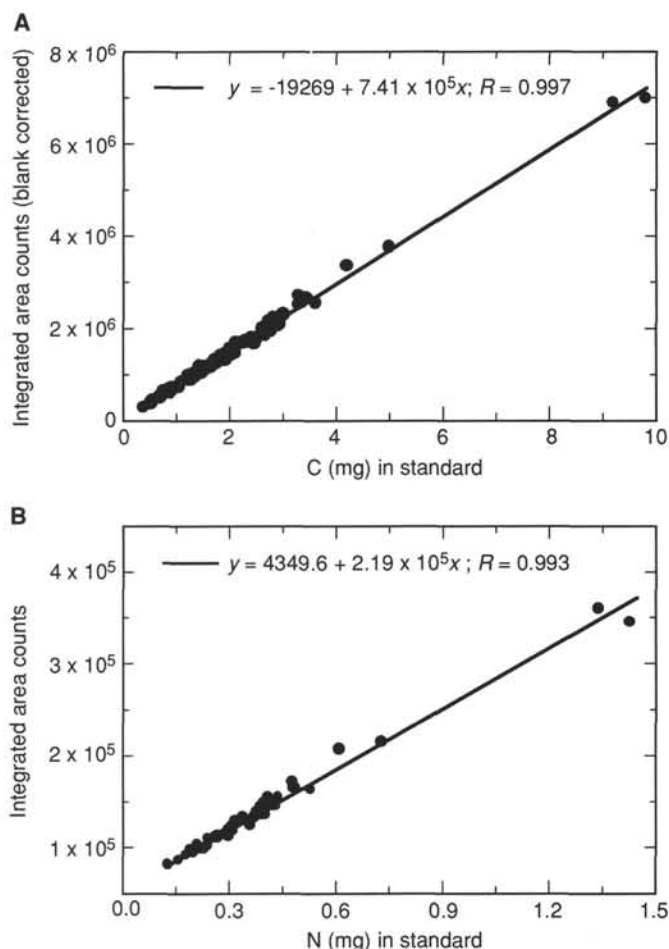


Figure 10. Linearity of the detector response of the CNS elemental analyzer at various concentrations of (A) carbon and (B) nitrogen in standard substances.

inorganic carbon (determined by coulometric analysis). We estimated the standard deviation of the analysis as <0.12% C_{org} based on the square root of the sum of squared standard deviations of total carbon (standard deviation = 0.08) and inorganic carbon (standard deviation = 0.09) determinations of calcium carbonate. Duplicate analyses with a set of 26 samples from Hole 847B indicate that concentrations of organic carbon were reproducible to within 0.2% C_{org}.

Residue Method

Because the error of organic carbon measurements using the difference method was greater than the actual concentrations of organic carbon in many samples from the western transect, we decided to determine organic carbon for these sites by analyzing the residue of inorganic carbon determinations. The resulting HCl-insoluble residue was centrifuged at 2000 to 2800 rpm for 5 to 10 min, and the supernatant was decanted. We washed the residue with approximately 2 mL nanopure water and repeated the centrifugation from one to three times. After the final decanting, the residues were dried overnight at 70° C, homogenized, and measured for carbon and nitrogen content in the CNS elemental analyzer. Concentrations in the residue were corrected for carbonate content by

$$(100 - \%CaCO_3) / (100 \cdot \%C_r),$$

where %C_r denotes carbon in the residue. Duplicate measurements of both CaCO₃ and carbon in the resulting residue of 16 samples from Sites 852 and 853 suggest that the method has good reproducibility

(range = 0.01%, standard deviation = 0.01%) at concentrations of C_{org} below 0.3%. The advantage of this technique is its tolerance to two major sources of error: inaccuracy when measuring inorganic carbon and inaccuracy when calibrating the total carbon technique. We stress that when using this method, it is very important that one correct adequately for blanks in the total carbon analysis. Even if we cannot quantify the loss of organic carbon through hydrolysis during acid treatment, the method has the distinct advantage of never yielding negative organic carbon numbers, which is an annoying attribute of the difference method at low C_{org} and high carbonate concentrations.

Gas Analysis

We took samples for gas analysis from each core in one of the holes (usually Hole B) drilled at a site. Normally, 5-cm³ samples were taken on the catwalk from the last undisturbed and complete section recovered (usually Section 6) before acetone was used to secure end caps to the section. Vials of 22-cm³ volume were filled with a known amount of sediment, sealed with a septum and a crimping tool, and heated for 2 hr at 70°C. The released gas was withdrawn by syringe and analyzed by gas chromatography (GC).

We used a different approach at Site 844, where sediment samples were prepared by the phase partitioning technique for detailed gas analysis and to obtain adequate amounts of gas for subsequent isotope analysis. Sediment samples of 40 to 50 cm³ were placed into a 290-cm³ glass jar, and 200 mL of distilled water was added. The jar then was covered with plastic film and sealed with a cap that had been fitted with a vacutainer septum. The assembled jar was vigorously shaken from 20 to 40 min to completely disaggregate the sample and to permit the interstitial gas to be redistributed between the solid/water/gas phases. For GC analysis, gas was collected by syringe through the septum in the cover of jar. The amount of gas was quantified from the concentration of gas in the injection (in ppm) and a multiplication factor m , taking into account the volumes of sediment (V_{sed}), water (V_{water}), and headspace (V_{hdsp}):

$$m = V_{\text{hdsp}}/V_{\text{sed}} \text{ and}$$

$$V_{\text{hdsp}} = V_{\text{jar}} - V_{\text{water}} - V_{\text{sed}}$$

An equal volume of headspace and sediment may be chosen; then, m equals unity. Because the amount of gas released from sediments at Site 844 was insufficient for isotope analysis, we abandoned this technique after this site.

Gas Chromatography and Quantification

At Site 844, gas samples were analyzed with Hewlett-Packard 5980A gas chromatograph equipped with a 6-ft \times 1/8-in. steel column packed with Poropak T, a 3-ft \times 1/8 in. steel column packed with 80/100 mesh HayeSep R(AW), and a DB1 fused silica capillary column (60 m \times 0.32 mm i.d., film thickness of 1 μ m). The chromatograph is equipped with a set of valves that splits gas flow between flame ionization (FID) and thermal conductivity (TCD) detectors. Using different combinations of these valves, one can select a sequence of columns to be most appropriate for the given GC analysis. After Site 844, most of the gas samples were analyzed with a Hach-Carle AGC Series 100 Model 211 gas analyzer equipped with a flame-ionization detector and a 6-ft \times 1/8-in. steel column packed with Poropak N:Q (80%:20%). This chromatograph provides fast and accurate analysis when methane concentrations are as low as those observed at all sites drilled during Leg 138.

The chromatographs were calibrated using standard gases of known composition. Under proper calibration, the computerized integrator provides concentrations (in ppm) of individual hydrocarbons in the gas analyzed. The concentration of hydrocarbons (in ppm) in

headspace volumes was then converted to μ L/L of sediment through the following formula:

$$C_{\text{gas}} = (a - b)V/v,$$

where

C_{gas} = the concentration of a hydrocarbon in the sediment in μ L/L,

a = the gas concentration (in ppm) measured in the gas chromatograph,

b = a background,

V = the volume of the vial used for headspace analysis, and

v = the volume of the sediment sample.

During previous legs, headspace analysis was used mainly as a monitoring technique for safety purposes. However, our experience has shown that the thermal desorption technique may provide accurate and reproducible data that are adequate for geochemical interpretation, if the following requirements are fulfilled: (1) all samples should be heated for the same amount of time (2 hr) and at the same temperature (70°C); (2) sealed vials filled with air should be run as blanks to quantify background; and (3) the volume of the sediment placed into the vial, from which gas is released, must be carefully measured.

Mass Accumulation Rates

Instantaneous mass accumulation rates (MARs) of bulk sediment, CaCO_3 , non- CaCO_3 , and organic carbon (C_{org}) were calculated for each sample. In addition to instantaneous MARs, average MARs of these four sedimentary components were calculated for the intervals delimited by the chronostratigraphic control points defined at each site (see "Sedimentation Rates" section, this chapter). All MARs are reported in $\text{g/cm}^2\text{-k.y.}$, except for C_{org} , which is reported in $\text{mg/cm}^2\text{-k.y.}$ MARs were calculated as the product of the concentration of the particular sedimentary component, the linear sedimentation rate (LSR) in cm/k.y. , and the dry bulk density (DBD) in g/cm^3 . For example, the CaCO_3 MAR is calculated as

$$\text{CaCO}_3 \text{ MAR (g/cm}^2\text{-k.y.)} = \% \text{CaCO}_3 \cdot \text{LSR (cm/k.y.)} \cdot \text{DBD (g/cm}^3\text{)/1000.}$$

An instantaneous LSR was calculated for each sample by linear interpolation between the chronostratigraphic control points (see "Sedimentation Rates" section, this chapter). The DBD of each physical property sample was measured directly (see "Physical Properties" section, this chapter) and is reported in each site report. For the remaining samples, a DBD was estimated either from the nearest measured value in the hole or from the $\% \text{CaCO}_3$ value based on a regression of the measured DBD vs. the $\% \text{CaCO}_3$ (see "Organic Geochemistry" section, "Site 844" chapter, this volume).

We stress that MARs are strongly controlled by LSR changes, and less so by changes in $\% \text{CaCO}_3$ or DBD. In absolute values, the variations in LSR generally are greater than those in $\% \text{CaCO}_3$ and DBD. For example, at Site 849, the range in the mean values of LSR, $\% \text{CaCO}_3$, and DBD were, respectively, 12.5–106.4 m/m.y., 50.4%–79.5%, and 0.61–0.88 g/cm^3 (see Table 12, "Organic Geochemistry" section, "Site 849" chapter, this volume). Clearly, the nine-fold range in LSR exerts a much greater influence on CaCO_3 MAR than the one- to two-fold differences in $\% \text{CaCO}_3$ and DBD. Therefore, the quality of the CaCO_3 MAR estimate is closely linked to the quality and detail of the LSR. In turn, the LSR depends on quality and resolution of the chronostratigraphy. The chronostratigraphy and the MARs presented herein will undoubtedly be revised on the basis of future work. Nonetheless, meaningful intersite comparison of the sedimentary records in the time domain is possible with the present stratigraphic

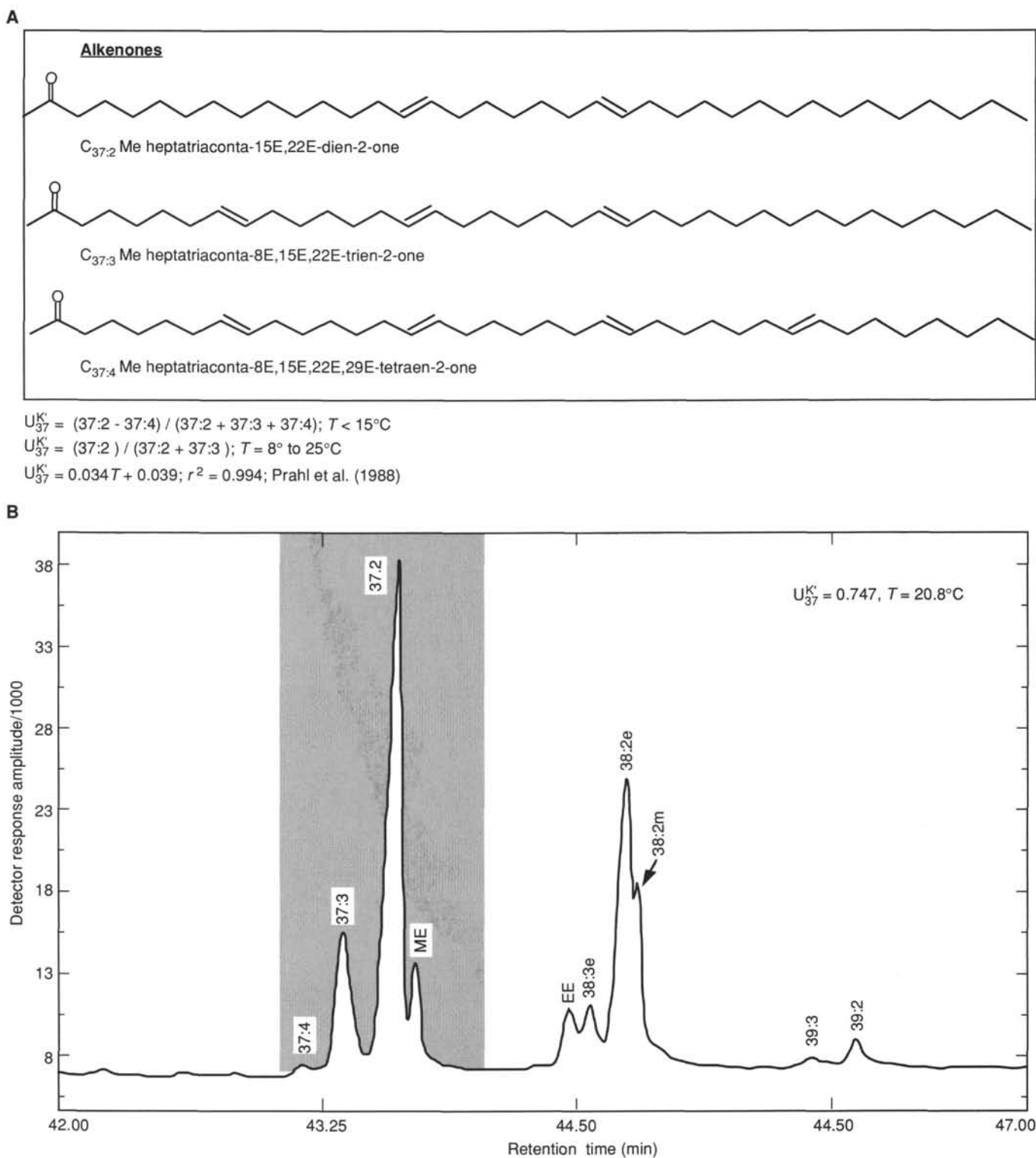


Figure 11. **A.** Schematic representation of alkenone structures and definition of the U_{37}^K index. **B.** Partial gas chromatogram of Sample 138-846D-1H-2, 40–42 cm, showing the retention times and peak characteristics of ketones of 37, 38, and 39 carbon atoms. Nomenclature after Prahl et al. (1988).

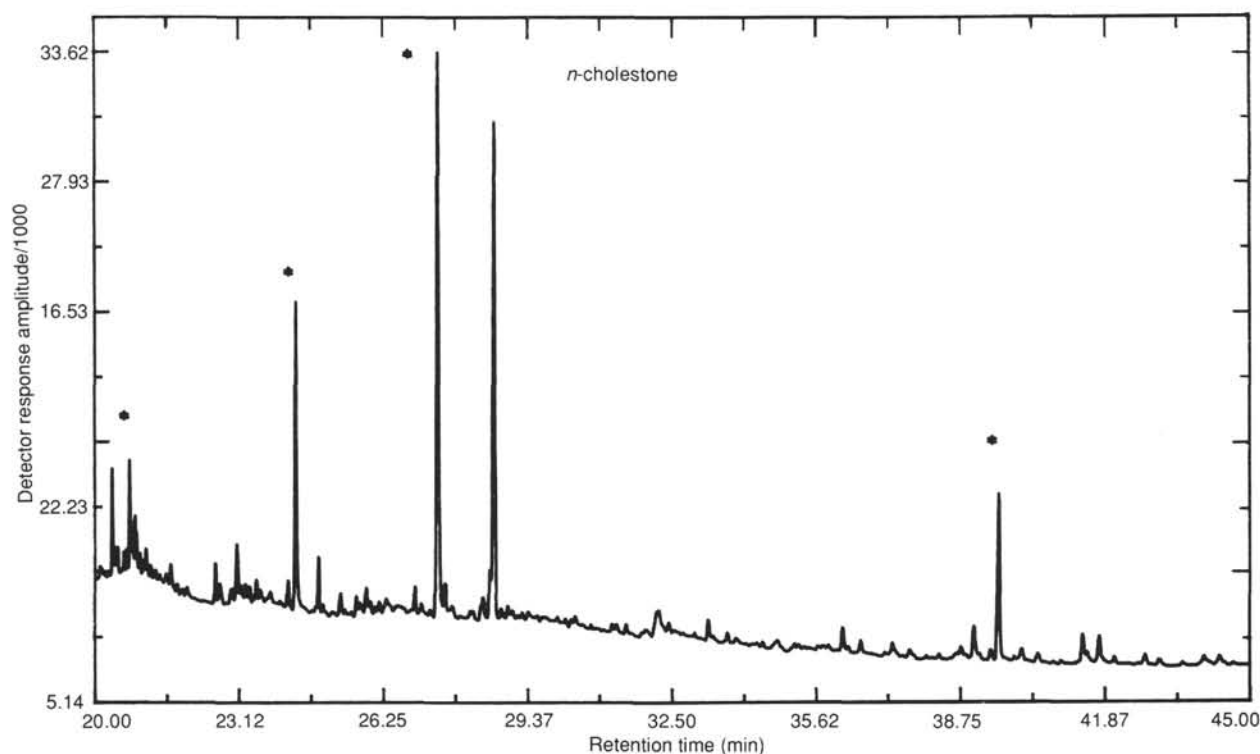


Figure 12. Gas chromatogram of a procedural blank of 10 mL methylene chloride, 5 mL hexane, and *n*-cholestane addition (5.6 μ L of 25 ng/ μ L standard solution). Peaks labeled with an asterisk are contaminants.

framework. During shipboard work, relatively detailed correlations among the sites already were established, but the first-order structures in the MAR records will most likely undergo subsequent revisions.

Lipids

To meet the objective of intercalibrating different methods of sea-surface temperature reconstructions, we measured the abundances of long-chain di- and tri-unsaturated alkenones in lipid extracts of samples from the top 40 m of sedimentary section at Site 846. The ratio of these components (see Fig. 11) has been established as a faithful indicator of variations in sea-surface temperature of the late Pleistocene (e.g., Brassell et al., 1986; Prahel et al., 1988). For extraction and analysis, we used procedures discussed next.

All glassware (centrifuge tubes, Pasteur pipettes, and boiling flasks) was thoroughly cleaned before extraction following the sequence: tap water, deionized water and soap, deionized water, nanopure water, oven dry at 80°C, rinse twice with methanol/toluene 1:1, rinse once with hexane. Sediment samples were lyophilized, ground with an agate mortar, and homogenized. Concentrations of CaCO₃, total nitrogen, total carbon, and organic carbon in the residues from carbonate analyses were measured in aliquots (see above for methods). Approximately 2 g of sediment was weighed into pre-cleaned centrifuge tubes. These samples were spiked with between 5 and 9 μ L of cholestane standard (25 ng/ μ L) to monitor extraction efficiency. Ten mL of methylene chloride (HPLC-GC-MS grade, Fisher Scientific) was added; the centrifuge tubes were capped with solvent-rinsed aluminum foil, placed into an ultrasonic bath, and ultrasonicated for 30 min. After centrifuging at 2000 rpm for 10 min, the solvent was decanted through hexane-rinsed disposable filtration column-filtering tubes (Baker) into pre-cleaned boiling flasks with glass stoppers. The extraction steps were repeated with 5 mL of hexane (HPLC-grade, Fisher Scientific), and the solvent fractions were combined.

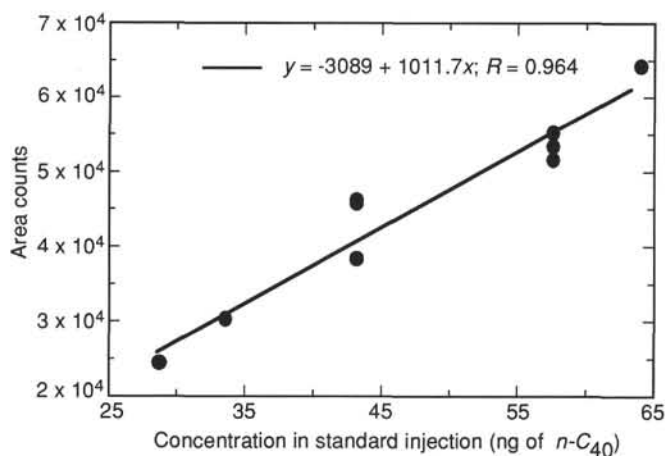


Figure 13. Calibration curve of injections of a standard mixture of *n*-C₄₀ used to quantify alkenone abundances.

The combined solvent fractions were evaporated to dryness under vacuum in a rotary evaporator at ambient temperature.

Hexane was added twice in quantities of 1 mL to the boiling flask containing the extracted lipids, then maneuvered to take up the lipids and to transfer them into pre-cleaned 2-mL glass screw-top vials. The transferred solvent and solutes were blown dry at 40°C under helium, 100 μ L of hexane was added, and the samples were placed in a refrigerator until analysis with the gas chromatograph.

We found that the on-board solvents (and methylene chloride in particular) were contaminated with components that are GC amenable, but that do not interfere with the analysis of the alkenones of interest. A gas chromatogram of a procedural blank, including cholestane

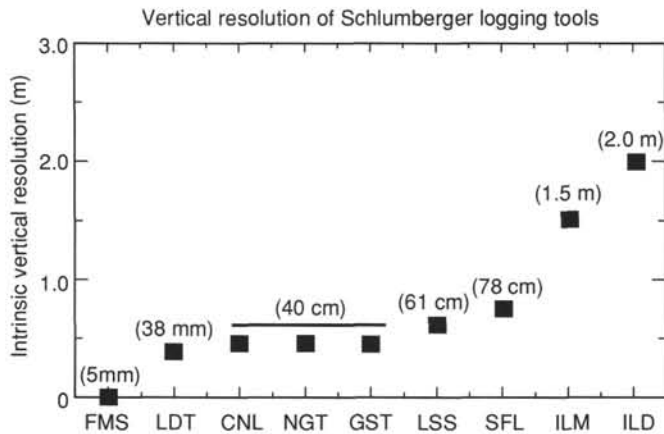


Figure 14. Vertical resolution of Schlumberger logging tools. FMS = formation microscanner; LDT = lithodensity tool; CNL = compensated neutron log; NGT = natural gamma-ray spectrometry tool; GST = gamma-ray spectrometry tool; LSS = long-spaced sonic tool; SFL = spherically focused log; ILM = phasor induction (medium); ILD = phasor induction (deep).

internal standard, 100 mL methylene chloride, and 5 mL hexane, is shown in Figure 12.

The shipboard gas chromatograph (Hewlett-Packard Model 5890A gas chromatograph) is equipped with a capillary column and a split/splitless injector system and was set up to optimize separation and quantitation of long-chain moieties having retention times >40 min. We chose the operating parameters discussed next.

The column was fused silica (cross-linked methyl silicone, 0.11 μm film thickness, 0.2-mm i.d., 25-m length) operated with helium as the carrier gas. Column head pressure was set to 200 kPa, translating into a linear flow velocity of 22 cm/s and a total flow of 0.75 cm^3/min . The injection system was operated in split mode with septum purge set to 4 mL/min. The injector temperature was 250°C to prevent septum pyrolysis, and septum purge was accomplished after 0.8 min. Detector (flame ionization detector) temperature was set to 300°C. The GC was programmed for the following temperature steps: 35°C for 2 min, followed by a ramped temperature of 10°C/min to 200°C, isothermal for 1 min, 4°C/min to 320°C, and isothermal for 5 min. Injection usually was below 6 μL of the sample drawn after hexane (1 μL) and air (1 μL), and followed by air.

Having established retention times and detector responses of the di- and tri-unsaturated alkenones by injection of pure synthetic standards (courtesy of G. Eglinton, Bristol), we quantified the recovered amount of alkenones per gram of sediment, considering the detector response to a standard solution of *n*-C₄₀ alkane standard (16 ng/ μL), the injected amount of sample, dilution, and sample weight (see Fig. 13). Each sample run was recorded on the HP laboratory automation system and was subsequently quantified after background was manually adjusted and peak integration. Duplicate injections afforded reasonable reproduction. Extraction efficiency was monitored by the abundance of cholestane in the samples and was found to be better than 80% with our extraction procedure. The net peak areas of C_{37:3} Me and C_{37:3} Me (see Fig. 11B) were transformed into the well-known ratio, U_{37}^K (C_{37:2} Me / (C_{37:2} Me + C_{37:3} Me)), which correlates well with and has been calibrated to growth temperature of coccolithophores in the marine environment and in laboratory cultures (e.g., Brassell et al., 1986; Prahl et al., 1988).

PHYSICAL PROPERTIES

Shipboard measurements of physical properties provide information that aids in the characterization of lithologic units, correlation of lithology with downhole geophysical logging results, and in the interpretation of seismic reflection and other geophysical data. The

goal of the physical properties program of Leg 138, in addition to providing a link between lithologic and geophysical data, was to identify the physical signals in the sediments that result from paleoceanographic change and diagenesis.

Several types of measurements were performed on the whole-round core sections. Measurements of bulk density, compressional-wave velocity, and magnetic susceptibility were provided by the MST. The MST incorporates the GRAPE, a compressional-wave core logger (PWL), and a magnetic susceptibility monitor (MSM). Thermal conductivities were measured using the needle-probe method at discrete intervals in whole-round sections.

Physical properties measured in samples obtained from the split cores included (1) vane shear strength, (2) compressional-wave velocity and attenuation, and (3) the index properties wet-bulk density, dry-bulk density, grain density, water content, porosity, and void ratio. Samples were chosen as representative of the core or section in undisturbed sediment. Measurements and samples were obtained generally at the frequency of two per section.

Multisensor Track

The MST incorporates the GRAPE, *P*-wave logger, and magnetic susceptibility devices. Individual unsplit core sections were placed horizontally on the MST and automatically moved through the three sets of sensors.

The GRAPE determines bulk density at intervals of 2 cm by comparing attenuation of gamma rays through the cores with attenuation through an aluminum standard (Boyce, 1976). GRAPE data are most reliable in APC cores. Drilling slurry between XCB "biscuits" gives lower bulk densities, and thus GRAPE data in XCB cores may be used only as an indication of trends and peaks in bulk densities. GRAPE data are useful for correlating between holes and sites by observing peak-to-peak spacings and general trends in the data.

The PWL transmits a 500-kHz compressional-wave pulse through the core at a repetition rate of 1 kHz. The transmitting and receiving transducers are aligned perpendicular to the core axis. A pair of displacement transducers monitors the separation between the compressional wave transducers; variations in the outside diameter of the liner thus do not degrade the accuracy of the velocities. Measurements are taken at 2.5-cm intervals. Generally, only the APC cores were measured, because the XCB and RCB cores often have voids between the core and the liner that cause transmission losses. Weak returns with signal strengths below a threshold value of 100 were removed.

The MST magnetic susceptibility procedures are included in the "Paleomagnetism" section (this chapter).

Thermal Conductivity

Thermal conductivity measurement techniques used during Leg 138 are described by Von Herzen and Maxwell (1959) and Vacquier (1985). Measurements were taken with a Thermcon-85 unit; all data are reported in units of W/(m · K). The estimated error in the measurements is about 5% to 10%. All data were corrected for *in-situ* pressure and temperature (Ratcliffe, 1960), assuming hydrostatic pressure and a conductive thermal gradient of about 35°C/m.

To reduce background thermal transients, cores were allowed to equilibrate in their liners until sediments reached a stable temperature. Needle probes were inserted in Sections 3 and 5 of every soft-sediment section through holes drilled in the liners. Sample temperatures were monitored with the thermistors in the probes, without applying a current to the heater wires. The actual test sequence began once the background temperature drift in was reduced to 0.04°C/min. Thermal conductivity is calculated from the rate temperature increases in the probe while a heater current is flowing. The increase in temperature in the probe should vary logarithmically with time as

$$T(t) = (q/4\pi k) \ln(t) + \text{const.}$$

where k = the thermal conductivity, T and t are the temperature and time, respectively, and q is the heat generated per unit length of the probe. Thermal conductivity can be derived from the slope of temperature vs. the logarithm of time. Thermal conductivities were measured until sediments became too lithified to insert the needle probes.

Vane Shear Strength

Undrained shear strengths of the sediment were determined using the Wykeham-Farrance vane shear device following Boyce's procedures (1976). The vane rotation rate was 89°/min. The vane (used for all measurements) has a 1:1 blade ratio with a dimension of 1.27 cm. A thorough discussion has been presented by Boyce (1976). When analyzing vane tests, one assumes that a cylinder of sediment is uniformly sheared about the axis of the vane in an undrained condition and that cohesion is the principal contributor to shear strength. Departures from this assumption include (1) progressive cracking within and outside of the failing specimen, (2) uplift of the failing core cylinder, (3) drainage of local pore pressures (i.e., the test can no longer be considered to be undrained), and (4) stick-slip behavior. In addition, silts and sands provide increased friction effects. In light of these problems (and because of the expected disturbance during drilling), the minivane test cannot be considered a measure of the true shear strength of the sediment. In a laboratory situation, only properly controlled triaxial or simple shear tests can be used to provide *in-situ* strength adequately. However, the minivane test does provide an estimate of strength and a means of comparing downcore with between-hole parameters.

Compressional-Wave Velocity

During Leg 138, compressional-wave (P -wave) velocities were measured using two different systems, depending on the degree of lithification of the sediment. Compressional-wave velocities were measured in unconsolidated sediment using a digital sound velocimeter (DSV; Mayer et al., 1987; Courtney and Mayer, in press). Calculation of velocity is based on the accurate measurement of the time of flight of an impulsive acoustic signal travelling between a pair of piezoelectric transducers inserted in the split sediment cores. The signal used is a 2- μ s square wave; the transducers have resonances at about 250 and 750 kHz. A dedicated microcomputer controls all functions of the velocimeter. The transmitted and received signals are digitized by a Nicolet 320 digital oscilloscope and transferred to the microcomputer for processing. The DSV software selects the first arrival and calculates sediment velocity; the complete waveform is stored for calculating attenuation later. During Leg 138, however, complete waveform data were not stored.

Four transducers are used: two of them, separated by approximately 7 cm, measure the vertical (along the core axis) compressional-wave velocity, while the other two, separated by approximately 3.5 cm, measure the horizontal (parallel to bedding). The transducers are firmly fixed at one end onto a steel plate so that their separation does not change when determining velocity. Thermistors in the transducer probes monitor temperature during measurement.

Periodically, the separation is evaluated precisely by running a calibration procedure in distilled water. A value of sound velocity in distilled water is determined (based on standard equations) for the measured temperature, while the computer calculates the transducer separation using the signal traveltime. At each sampling interval (usually two per section), the transducers were inserted carefully into the split section and velocity was measured in both directions.

The Hamilton Frame velocimeter was used to measure compressional-wave velocities at 500 kHz in discrete sediment samples when (1) induration made it difficult to insert the DSV transducers without making any perturbations around them and (2) in lithified sediments when insertion became impossible. Samples were carefully cut using

a double-bladed diamond saw. Sample thicknesses were measured directly from the velocimeter-frame lead screw. Zero traveltimes for the velocity transducers were estimated by linear regression of traveltime vs. distance for a series of aluminum and lucite standards. Filtered seawater was used to improve the acoustic contact between the sample and the transducers. The DSV oscilloscope and processing software were used to digitize waveforms, to calculate velocities, and to store the waveforms for calculating attenuation later.

Index Properties

Index properties (bulk density, grain density, water content, porosity, and dry density) were calculated from measurements of wet and dry weights and of dry volume. Samples of approximately 10 cm³ were taken to determine index properties. Soft-sediment samples were placed in pre-calibrated aluminum containers before measuring weight and volume. Index properties for lithified sediment and basement rock samples were measured on crushed portions of the sample cubes that had been cut to determine velocity.

Sample weights were determined aboard the ship to a precision of ± 0.01 g using a Scitech electronic balance. Volumes were determined using a Quantachrome penta-pycnometer, a helium-displacement pycnometer. The Quantachrome pycnometer measures volumes to an approximate precision of 10⁻⁴ cm³.

Scientists have observed that the frequent decreases in air pressure in the ship's laboratories affect the performance of this pycnometer. Another problem in consistency arises as a result of slightly different pressures measured during different calibration runs. The variability associated with decreased pressure was minimized by repeating the measurements until two volumes for the same cell agreed to within 0.05 cm³. To correct for the differences associated with changes in calibration pressure, a standard was included in every other pycnometer run. The standard was rotated through each of the cells so that changes in the cells could be monitored. Sample volumes then were corrected for deviations from the known standard volume.

At the first site, both wet and dry volumes were measured for each sample. We soon saw that to keep up with the desired sampling frequency, samples from subsequent sites could be run through the pycnometer only once. Examination of data indicated that the dry volumes measured with the pycnometer were more accurate than the wet volumes, a result of the presence of volatiles in the wet samples that causes erroneous pressure readings. Therefore, for subsequent sites, only dry samples were run through the pycnometer. Dry weights and volumes were measured after the samples were oven-dried at 110°C for 24 hr and allowed to cool in a desiccator. A salt correction

Table 9. Abbreviations used in "Downhole Measurements" sections.

Abbreviation	Definition
Mbsf	Meters below seafloor
Mbrf	Meters below rig floor
Fbrf	Feet below rig floor
RIH	Run into hole
POOH	Pull out of hole
TD	Total depth (bottom of hole)
NGT	Natural gamma-ray tool
DIT	Phasor dual induction tool
HLDT	High-temperature lithodensity tool
LSS or SDT	Long-spaced sonic digital tool
TLT	LDGO temperature logging tool
FMS	Formation microscanner
GPIT	General purpose inclination tool
ACT	Aluminum clay tool
GST	Geochemical spectral tool
BHC	Borehole compensated sonic tool
API units	American Petroleum Institute standard unit for gamma-ray activity based upon calibration in standard well in Houston.

(assuming 35 ppt interstitial fluid salinity) was applied to density and porosity computations as per Hamilton (1971).

Wet bulk density was calculated from both wet and dry weights and dry volumes. The wet volume (V_w) was calculated by adding the weight of the water lost through drying of the sample to the dry volume, using the following equation:

$$V_w = V_d + (W_w - W_d)/\rho_f$$

where ρ_f = the density of evaporated water and is assumed to equal 1, W_d = weight of dry sediment, and W_w = weight of wet sediment. The dry volume, V_d , includes both the volume of the sediment or rock constituents and the volume of salt remaining in the sample after drying. Then, the wet bulk density is calculated in the normal manner, as follows:

$$\rho_{bw} = W_w/V_w$$

Porosity, water content (calculated as a percentage of dry weight), grain density, and dry bulk density also were calculated using this calculated wet volume, according to the equations of Boyce (1976).

DOWNHOLE MEASUREMENTS

General

During Leg 138, the downhole logging program was designed to characterize the geophysical, geochemical, and structural properties of the sedimentary deposits encountered at each site. Following completion of coring, a combination of logging tools are formed into "strings" and lowered into the borehole on a seven-conductor cable; each of the measuring devices continuously monitors properties of the formation. Data are typically recorded at 15-cm intervals. Vertical resolution of the data varies, depending on the tool (Fig. 13). Three tool strings of Schlumberger sensors were used during Leg 138: (1) the geophysical tool string, (2) the geochemical tool string, and (3) the formation microscanner (FMS). In addition, the Lamont-Doherty temperature tool was attached to the base of each tool string.

Depths in logs (measured by wireline) may not exactly match depths in cores measured by the drill string. Every attempt was made to match the two, but some residual differences may have remained. All logs were depth-matched to each other by correlating the natural gamma-ray activity profiles from each logging run.

Geophysical Tool String

The geophysical tool string used during Leg 138 comprises four sensors: (1) the natural gamma-ray spectrometry tool (NGT) (see Table 9); (2) the phasor dual-induction tool (DIT), (3) the long-spacing digital sonic tool (SDT), and (4) the high-temperature lithodensity tool (HLDT). The geophysical tool string is designed to measure compressional-wave velocity, deep, intermediate, and shallow resistivities, and the formation density. Sonic velocity data are combined with density measurements to calculate an impedance log and to generate synthetic seismograms for the logged sequence. The NGT is run on all three tool strings to provide a common basis for log correlations.

The DIT provides three measurements of electrical resistivity, all with different radial depths of investigation. Two induction devices ("deep" and "medium" resistivities) send high-frequency alternating current through transmitter coils, creating a magnetic field that induces a secondary (Foucault) current in the formation. This ground-loop current produces a new inductive signal that is proportional to the conductivity of the formation. This inductive signal is recorded by a series of receiving coils and is then converted to resistivity values. A third device, the "spherically focused" resistivity tool (SFLU),

measures the current necessary to maintain a constant voltage decrease across a fixed interval. The vertical resolution is of the order of 2 m for the two former devices and approximately 0.7 m for the SFLU. The data can be corrected for irregularities in borehole diameter.

Resistivity is a function of the inverse square root of porosity (Archie, 1942). Fluid salinity, clay content, hydrocarbon content, and temperature also are important influences on electrical resistivity. Other factors that may affect the measured resistivity are the concentration of hydrous and metallic minerals, formation vesicularity, and the geometry of the pore space.

The SDT records the time required for sound to travel along the borehole wall from one of two acoustic transmitters to two receivers over source-receiver distances of 8, 10, and 12 ft (2.4, 3.0, and 3.6 m). First arrivals for the individual source-receiver paths are used to calculate sonic velocities; four velocity values are measured at each depth, along four possible paths. Only compressional-wave velocities are determined on board the ship, but complete sonic waveforms are recorded for post-cruise processing to determine shear wave and Stoneley wave velocities. The vertical resolution of the tool is approximately 2 ft (0.61 m). Logs can be corrected for cycle skipping—where the receiver misses the first arrival and responds to that of the second signal—using the four-way measurement redundancy. Compressional-wave velocity is controlled primarily by porosity and lithification; decreases in porosity and increases in consolidation and lithification typically result in velocity increases with depth in a sedimentary deposit.

The HLDT uses a 0.66 MeV ^{137}Ce gamma-ray source for measuring density. The source is mounted in the tool body; an eccentricizing caliper presses it and a pair of detectors against the borehole wall. Determination of density is based on Compton scattering of the gamma rays within the formation and is a measure of electron density. Electron density can be converted to bulk density because most rock-forming elements have atomic weights that are twice their atomic numbers. In addition, the HLDT records a photoelectric effect index. Photoelectric absorption occurs in the energy window below 150 KeV and is dependent upon the energy of the incident gamma rays, atomic cross section, and the nature of the atom. The measurement is independent of porosity and thus can be used as a matrix lithology indicator. Density and photoelectric effect measurements require good contact between the sensor and borehole wall; the tool measures this contact and corrects for excessive borehole roughness. The vertical resolution of the tool is approximately 0.5 m.

Geochemical Tool String

The geochemical tool string used during Leg 138 included an NGT, an induced gamma-ray spectroscopy tool (GST), and an aluminum clay tool (ACT). Relative concentrations of Si, Ca, Fe, S, H, and Cl and weight percentages of K, U, Th, and Al were determined on board the ship. Additional shore-based processing will be required to obtain weight abundances of the first six elements, plus Gd and Ti.

The NGT measures the natural radioactivity of the formation. The majority of natural gamma rays are emitted by ^{40}K and by U and Th isotopes and their daughter products. The near-field (i.e., near the borehole wall) natural gamma-ray emissions of the formation are measured by an NaI scintillation detector mounted inside the sonde. The energy spectrum measured by the detector is divided into five discrete energy windows. The total counts recorded in each window, for a specific depth in the borehole, are processed to give elemental abundances of K, U, and Th. The depth of investigation is about 0.3 to 0.5 m. The NGT data have been corrected for variations in borehole diameter. This tool is run on each combination tool string to provide a basis for depth correlations among runs.

K, U, and Th generally are most abundant in clay minerals (vs. biogenic opal or calcite, for example); thus, the gamma-ray log is commonly used as an estimate of the clay content of the formation.

However, silicic volcanoclastic material and K-feldspar-rich rocks can also have high concentrations of these three elements, so interpretations must be tied to the core lithology.

The GST consists of a pulsed 14-MeV neutron generator and an NaI scintillation detector. Incident neutrons lose energy through inelastic scattering in the formation and eventually are captured by elemental nuclei when they reach thermal levels (approximately 0.02 eV). After capture, gamma rays are emitted by the capture atoms; these gamma rays are detected by the tool. The 256-channel energy spectrum is deconvolved to determine relative abundances of Ca, Si, Fe, Cl, H, and S on board the ship. These raw data are later subjected to extensive post-cruise reprocessing by the Borehole Research Group at Lamont-Doherty Geological Observatory to produce weight percentages of these elements and of Gd and Ti.

Aluminum abundance is obtained with the ACT. When Al absorbs a neutron from the 2.5 MeV ^{252}Cf source of the ACT, it forms an unstable nucleus with a half-life of about 2 min. When the unstable nucleus decays, a gamma ray with a characteristic energy is emitted and detected by the NGT. The induced gamma-ray activity is isolated by removing the gamma-ray spectrum that results from natural radiation by running NGT tools above and below the neutron source. The detector above measures natural radiation before activation; the detector below measures the induced radiation.

Formation Microscanner

The FMS produces high-resolution images of the microresistivity character of the borehole wall. These images may be used for detailed sedimentological and/or structural interpretations (Ekstrom et al., 1986; Pezard and Luthi, 1988).

The FMS tool comprises 16 electrode "buttons" on four orthogonal pads that are pressed against the borehole wall. The electrodes are spaced approximately 2.5 mm apart and are arranged in two diagonally offset rows of eight electrodes each. Processing corrects the offset rows to one level, doubling the horizontal resolution to approximately 1.25 mm. The FMS tool string contains a general purpose inclinometry tool (GPIT) that spatially orients the resistivity measurements via an accelerometer and measurement of the declination and inclination of Earth's magnetic field vector. In addition, the tool string includes an NGT to assist correlation of the FMS to other logs. The raw data are processed post-cruise to transform individual microresistivity traces into complete, spatially oriented images. Only limited processing can be accomplished at sea.

Possible applications of the FMS logs include (1) detailed correlation of coring and logging depths, (2) orientation of cores, (3) mapping of fractures, faults, foliations, and other formation structures, as well as (4) determination of strikes and dips of bedding planes. In addition, the FMS can be used to estimate stress in the borehole with precise measurements of borehole diameter in two orthogonal directions. In an isotropic, linearly elastic rock subjected to an anisotropic stress field, breakouts form along the borehole wall as a result of compressive stress that exceeds the strength of the rock. Under these conditions, the breakout orientation develops in the direction of the least principal horizontal stress. Stress orientations deduced from breakouts have been demonstrated to be consistent with other independent stress indicators (Bell and Gough, 1979; Zoback et al., 1988).

REFERENCES

- Alexandrovich, J. M., 1991. Stratigraphy, sedimentology, and paleoceanography of the eastern equatorial Pacific: late Miocene through Pleistocene [Ph.D. dissert.]. Columbia Univ., New York.
- Archie, G. E., 1942. The electrical resistivity log as an aid in determining some reservoir characteristics. *J. Pet. Tech.*, 5:1-8.
- Backman, J., and Pestiaux, P., 1986. Pliocene *Discoaster* abundance variations, Deep Sea Drilling Project Site 606: biochronology and paleoenvironmental implications. In Ruddiman, W. F., Kidd, R. B., Thomas, E., et al., *Init. Repts. DSDP*, 94 (Pt. 2): Washington (U.S. Govt. Printing Office), 903-910.
- Backman, J., Schneider, D. A., Rio, D., and Okada, H., 1990. Neogene low-latitude magnetostratigraphy from Site 710 and revised age estimates of Miocene nannofossils datum events. In Duncan, R. A., Backman, J., Peterson, L. C., et al., *Proc. ODP, Sci. Results*, 115: College Station, TX (Ocean Drilling Program), 271-276.
- Backman, J., and Shackleton, N. J., 1983. Quantitative biochronology of Pliocene and early Pleistocene calcareous nannofossils from the Atlantic, Indian and Pacific oceans. *Mar. Micropaleontol.*, 8:141-170.
- Baldauf, J. G., 1984. Cenozoic diatom biostratigraphy and paleoceanography of the Rockall Plateau Region, North Atlantic, Deep Sea Drilling Project Leg 81. In Roberts, D. G., Schnitker, D., et al., *Init. Repts. DSDP*, 81: Washington (U.S. Govt. Printing Office), 439-478.
- , 1985. A high resolution late Miocene-Pliocene diatom biostratigraphy for the eastern equatorial Pacific. In Mayer, L., Theyer, F., Thomas, E., et al., *Init. Repts. DSDP*, 85: Washington (U.S. Govt. Printing Office), 457-475.
- Barron, J. A., 1980. Upper Pliocene and Quaternary diatom biostratigraphy of Deep Sea Drilling Project Leg 54, tropical eastern Pacific. In Rosendahl, B. R., Hekinian, R., et al., *Init. Repts. DSDP*, 54: Washington (U.S. Govt. Printing Office), 455-485.
- , 1981. Middle Miocene diatom biostratigraphy of DSDP Site 77B in the eastern equatorial Pacific. *Geosci. J.*, 2:137-144.
- , 1983. Latest Oligocene through early middle Miocene diatom biostratigraphy of the eastern tropical Pacific. *Mar. Micropaleontol.*, 7:487-515.
- , 1985a. Late Eocene to Holocene diatom biostratigraphy of the equatorial Pacific Ocean, Deep Sea Drilling Project Leg 85. In Mayer, L., Theyer, F., Thomas, E., et al., *Init. Repts. DSDP*, 85: Washington (U.S. Govt. Printing Office), 413-456.
- , 1985b. Miocene to Holocene planktic diatoms. In Bolli, H. M., Saunders, J. B., Perch-Nielsen, K. (Eds.), *Plankton Stratigraphy*: Cambridge (Cambridge Univ. Press), 763-809.
- , in press. Neogene diatom datum levels in the equatorial and north Pacific. In Saito, T., and Ishizaki, K. (Eds.), *The Centenary of Japanese Micropaleontology*: Tokyo (Tokyo Univ. Press).
- Barron, J. A., Keller, G., and Dunn, D. A., 1985. A multiple microfossil biochronology for the Miocene. In Kennett, J. P. (Ed.), *The Miocene Ocean: Paleocceanography and Biogeography*. Mem.—Geol. Soc. Am., 163:21-36.
- Bell, J. S., and Gough, D. I., 1979. Northeast-southwest compressive stress in Alberta: evidence from oil wells. *Earth Planet. Sci. Lett.*, 45:475-482.
- Berggren, W. A., Kent, D. V., and Van Couvering, J., 1985. The Neogene: Part 2. Neogene geochronology and chronostratigraphy. In Snelling, N. J. (Ed.), *The Chronology of the Geological Record*. Geol. Soc. London Mem., 211-260.
- Blow, W. H., 1969. Late middle Eocene to Recent planktonic foraminiferal biostratigraphy. In Brönniman, P. and Renz, H. H. (Eds.), *Proc. First Int. Conf. Planktonic Microfossils*, Geneva, 1967. Leiden (E. J. Brill), 1:199-422.
- Boyce, R. E., 1976. Definitions and laboratory determination of compressional sound velocity parameters and wet-water content, wet-bulk density and porosity parameters by gravimetric and gamma-ray attenuation techniques. In Schlanger, S. O., Jackson, E. D., et al., *Init. Repts. DSDP*, 33: Washington (U.S. Govt. Printing Office), 931-958.
- Brassell, S. C., Eglinton, G., Marlowe, I. T., Pflaumann, U., and Sarnthein, M., 1986. Molecular stratigraphy: a new tool for climatic assessment. *Nature*, 320:129196133.
- Bukry, D., 1973. Low-latitude coccolith biostratigraphic zonation. In Edgar, N. T., Saunders, J. B., et al., *Init. Repts. DSDP*, 15: Washington (U.S. Govt. Printing Office), 685-704.
- , 1975. Coccolith and silicoflagellate stratigraphy, northwestern Pacific Ocean, Deep Sea Drilling Project Leg 32. In Larson, R. L., Moberly, R., et al., *Init. Repts. DSDP*, 32: Washington (U.S. Govt. Printing Office), 677-701.
- Burckle, L. H., 1972. Late Cenozoic planktonic diatom zones from the eastern equatorial Pacific. *Nova Hedwegia Beih.*, 39:217-246.
- , 1977. Pliocene and Pleistocene diatom datum levels from the equatorial Pacific. *Quat. Res.*, 7:330-340.
- , 1978. Early Miocene to Pliocene diatom datum levels for the equatorial Pacific. *Proc. Second Working Group Mtg. Biostratigraphic Datum Planes Pacific Neogene, IGCP Proj. 114*. Spec. Publ., Geol. Res. Dev. Ctr. 1:25-44.
- Burckle, L. H., Keigwin, L. D., and Opdyke, N. D., 1982. Middle and late Miocene stable isotope stratigraphy: correlation to the paleomagnetic reversal record. *Micropaleontology*, 32:372-377.
- Burckle, L. H., and Trainer, J., 1979. Middle and Late Pliocene diatom datum levels from the central Pacific. *Micropaleontology*, 25:281-293.
- Courtrey, R. C., and Mayer, L. A., in press. Calculating acoustic parameter by a filter correlation method. *J. Acoust. Soc. Am.*

- Dunham, R., 1962. Classification of carbonate rocks according to depositional texture. In Ham, W. E. (Ed.), *Classification of Carbonate Rocks*. AAPG, 108–121.
- Ekstrom, M. P., Dahan, C. A., Chen, M.-Y., Lloyd, P. M., and Rossi, D. J., 1986. Formation imaging with microelectrical scanning arrays. *Trans. SPWLA 27th Ann. Logging Symp.*, Pap. BB.
- Fornaciari, E., Raffi, I., Rio, D., Backman, J., and Olafsson, G. 1990. Quantitative distribution patterns of Oligocene and Miocene calcareous nannofossils from the Western Equatorial Indian Ocean. In Duncan, R. A., Backman, J., Peterson, L. C., et al., *Proc. ODP, Sci. Results*, 115: College Station, TX (Ocean Drilling Program), 237–254.
- Gartner, S., 1977. Calcareous nannofossil biostratigraphy and revised zonation of the Pleistocene. *Mar. Micropaleontol.*, 2:1–25.
- Gieskes, J. M., and Peretsman, G., 1986. Water chemistry procedures aboard *JOIDES Resolution*—some comments. *ODP Tech. Note*, 5.
- Hamilton, E. L., 1971. Prediction of *in-situ* acoustic and elastic properties of marine sediments. *Geophysics*, 36:266–284.
- Hays, J. D., and Shackleton, N. J., 1976. Globally synchronous extinction of the radiolarian *Strylactrus universus*. *Geology*, 4:649–652.
- Johnson, D. A., and Nigrini, C. A., 1985. Synchronous and time-transgressive Neogene radiolarian datum levels in the equatorial Indian and Pacific Oceans. *Mar. Micropaleontol.*, 9:489–523.
- Johnson, D. A., Schneider, D. A., Nigrini, C. A., Caulet, J. P., and Kent, D. V., 1989. Pliocene-Pleistocene radiolarian events and magnetostratigraphic calibrations for the tropical Indian Ocean. *Mar. Micropaleontol.*, 14:33–66.
- Kennett, J. P., and Srinivasan, M. S., 1983. *Neogene Planktonic Foraminifera: A Phylogenetic Atlas*: Stroudsburg, PA (Hutchinson Ross).
- Kroenke, L. W., Berger, W. H., Janacek, T. R., et al., 1991. *Proc. ODP, Init. Repts.*, 130: College Station, TX (Ocean Drilling Program).
- Mankinen, E. A., and Dalrymple, G. B., 1979. Revised geomagnetic polarity time scale for the interval 0–5 m.y.B.P. *J. Geophys. Res.*, 84:615–626.
- Martini, E., 1971. Standard Tertiary and Quaternary calcareous nannoplankton zonation. In Farinacci, A. (Ed.), *Proc. 2nd Planktonic Conf. Roma*: Rome (Ed. Tecnosci.), 739–785.
- Mayer, L. A., Courtney, R. C., and Moran, K., 1987. Ultrasonic measurements of marine sediment properties. *Proc. Oceanogr.*, 87:1–139.
- Mazzullo, J. M., Meyer, A., and Kidd, R., 1987. New sediment classification scheme for the Ocean Drilling Program. In Mazzullo, J., and Graham, A. G., *Handbook for Shipboard Sedimentologists*. ODP Tech. Note, 8:45–67.
- Nigrini, C. A., 1971. Radiolarian zonation in the Quaternary of the equatorial Pacific Ocean. In Funnell, B. M., and Riedel, W. R. (Eds.), *The Micropaleontology of Oceans*: Cambridge (Cambridge Univ. Press), 443–461.
- Nigrini, C. A., and Caulet, J. P., 1988. The genus *Anthocyrtidium* (Radiolaria) from the tropical late Neogene of the Indian and Pacific Oceans. *Micropaleontology*, 34:341–360.
- Norrish, K., and Hutton, J. T., 1969. An accurate X-ray spectrographic method for the analysis of a wide range of geological samples. *Geochim. Cosmochim. Acta*, 33:431–453.
- Okada, H., and Bukry, D., 1980. Supplementary modification and introduction of code numbers to the low-latitude coccolith biostratigraphic zonation (Bukry, 1973; 1975). *Mar. Micropaleontol.*, 5:321–325.
- Olafsson, G. 1991. Quantitative calcareous nannofossil biostratigraphy and biochronology of early through late Miocene sediments from DSDP Hole 608. *Medd. Stockholms Univ. Inst. Geol. Geochem.*, 285:pap. 4.
- Pezard, P. A., and Luthi, S. M., 1988. Borehole electrical images in the basement of the Cajon Pass scientific drillhole, California: fracture identification and tectonic implications. *Geophys. Res. Lett.*, 15:1017–1020.
- Prahl, F. G., Muehlhausen, L. A., and Zahnle, D. L., 1988. Further evaluation of long-chain alkenones as indicators of paleoceanographic conditions. *Geochim. Cosmochim. Acta*, 52:2303–2310.
- Ratcliffe, E. H., 1960. The thermal conductivities of ocean sediments. *J. Geophys. Res.*, 65:1535–1541.
- Reynolds, R. C., 1967. Estimations of mass absorption coefficients by Compton scattering: improvements and extensions of the method. *Am. Mineral.*, 48:1133–1143.
- Rio, D., Backman, J., and Raffi, I., in press. Calcareous nannofossil biochronology and the Pliocene-Pleistocene boundary. In Van Couvering, J. (Ed.), *Final Repts., IGCP Project 41*.
- Rio, D., Fornaciari, E., and Raffi, I., 1990a. Late Oligocene through early Pleistocene calcareous nannofossils from western Equatorial Indian Ocean (Leg 115). In Duncan, R. A., Backman, J., Peterson, L. C., *Proc. ODP, Sci. Results*, 115: College Station, TX (Ocean Drilling Program), 175–235.
- Rio, D., Raffi, I., and Villa, J., 1990b. Pliocene-Pleistocene calcareous nannofossil distribution patterns in the Western Mediterranean. In Kastens, K. A., Mascle, J., et al., *Proc. ODP, Sci. Results*, 107: College Station, TX (Ocean Drilling Program), 513–533.
- Roth, P. H., 1983. Calcareous nannofossils—Leg 17, Deep Sea Drilling Project. In Winterer, E. L., Ewing, J. I., et al., *Init. Repts. DSDP*, 17: Washington (U.S. Govt. Printing Office), 695–795.
- Roth, P. H., and Thierstein, H. R., 1972. Calcareous nannoplankton: Leg 14 of the Deep Sea Drilling Project. In Hayes, D. E., Pimm, A. C., et al., *Init. Repts. DSDP*, 14: Washington (U.S. Govt. Printing Office), 421–485.
- Sancetta, C., 1984. Diatoms from Leg 75, Deep Sea Drilling Project. In Hay, W. W., Sibuet, J. C., et al., *Init. Repts. DSDP*, 75: Washington (U.S. Govt. Printing Office), 755–762.
- Sanfilippo, A., Westberg-Smith, M. J., and Riedel, W. R., 1985. Cenozoic radiolaria. In Bolli, H. M., Saunders, J. B., Perch-Nielsen, K. (Eds.), *Plankton Stratigraphy*: Cambridge (Cambridge Univ. Press), 631–712.
- Shackleton, N. J., Berger, A., and Peltier, W. R., 1990. An alternative astronomical calibration of the lower Pleistocene timescale based on ODP Site 677. *Trans. R. Soc. Edinburgh, Earth Sci.*, 81:251–261.
- Shipboard Scientific Party, 1985. Explanatory notes. In Mayer, L., Theyer, F., Thomas, E., et al., *Init. Repts. DSDP*, 85: Washington (U.S. Govt. Printing Office), 5–22.
- Solorzano, L., 1969. Determination of ammonia in natural waters by phenol-hypochlorite method. *Limnol. Oceanogr.* 14:789–801.
- Tauxe, L., Opydyke, N. D., Pasini, G., and Elmi, C., 1983. Age of the Plio-Pleistocene boundary in the Vrica Section, southern Italy. *Nature*, 304:125–129.
- Thierstein, H. R., Geitzenauer, K., Molino, B., and Shackleton, N. J., 1977. Global synchronicity of late Quaternary coccolith datum levels: validation by oxygen isotopes. *Geology*, 5:400–404.
- Tsunogai, S., Nishimura, M., and Nakaya, S., 1968. Complete metric titration of calcium in the presence of large amounts of magnesium. *Talanta*, 15:385–390.
- Vaquier, V., 1985. The measurement of thermal conductivity of solids with a transient linear heat source on the plane surface of a poorly conducting body. *Earth Planet. Sci. Lett.*, 74:275–279.
- Von Herzen, R. P., and Maxwell, A. E., 1959. The measurement of thermal conductivity of deep-sea sediments by a needle probe method. *J. Geophys. Res.*, 65:1557–1563.
- Weaver, P.P.E., and Clement, B. M., 1987. Magnetobiostratigraphy of planktonic foraminiferal datums: Deep Sea Drilling Project Leg 94, North Atlantic. In Ruddiman, W. R., Kidd, R. B., Thomas, E., et al., *Init. Repts. DSDP*, 94: Washington (U.S. Govt. Printing Office), 815–829.
- Wentworth, C. K., 1922. A scale of grade and class terms of clastic sediments. *J. Geol.*, 30:377–390.
- Zijderveld, J.D.A., Zachariasse, J. W., Verhallen, P.J.J.M., and Hilgen, F. J., 1986. The age of the Miocene/Pliocene boundary. *Newsl. Stratigr.*, 16:169–181.
- Zoback, M. D., Zoback, M. L., Mount, V. S., Suppe, J., Eaton, J. P., Healy, J., H., Oppenheimer, D., Reasenberg, P., Jones, L., Raleigh, C., Wong, I. G., Scotti, O., and Wentworth, C., 1988. New evidence on the state of stress of the San Andreas Fault. *Science*, 238:1105–1111.